Dust Entrainment by Rotor Downwash in Variable Pressure Environments

MSc Thesis Aerospace Engineering

R.M. van der Voort

Delft University of Technology

This page was intentionally left blank

Dust Entrainment by Rotor Downwash in Variable Pressure Environments

by

R.M. van der Voort

to obtain the degree of Master of Science
at the Delft University of Technology, Faculty of Aerospace Engineering,
to be defended publicly on Friday November 7, 2025 at 10:00 AM.

Student number:	4672356	
Research Department:	Space Engineering, section Planetary Exploration	
Project duration:	January 27, 2025 – November 7, 2025	
Thesis committee:	Dr. S. de Vet,	TU Delft, supervisor
	Prof. dr. L.L.A. Vermeersen,	TU Delft, chair
	Dr.ir. E.J.O. Schrama	TU Delft, external
External supervisor:	Lt-Kol E. Frijters,	Royal Netherlands Airforce, Center of Man and Aviation

Cover: ChatGPT generated picture using the prompt: ”Drawing of Rover Helicopter on Mars”

Summary

Rotor downwash that lifts dust from the ground, often called brownout on Earth, has long challenged safe rotorcraft operations. As flight moves from dense terrestrial air toward thin, planetary atmospheres, the physics change: the same rotor, at the same height, produces a very different near-surface flow. If the minimum conditions needed to mobilize dust grains and the effects of the dust once in motion are misjudged, landings, takeoffs, and low-altitude manoeuvrers can become unsafe, sensors can be degraded, and contamination risks can rise. Despite extensive understanding of brownout at Earth sea level, the physics of rotor-induced entrainment under reduced pressure remains poorly constrained.

This thesis addresses that gap by posing a focused objective: contribute to safer and more predictable rotorcraft operations in low-pressure environments by quantifying how the thresholds and the intensity of dust entrainment produced by rotor downwash evolve as ambient pressure is stepped from Earth-like toward Mars-like conditions. In other words, the work questions how the minimum surface shear required to start motion, and the strength of the dust once moving, change as the atmosphere thins.

To meet this objective, experiments are performed in a hypobaric chamber equipped with a test box and a single-rotor setup. Pressure is swept from roughly sea-level values down to tens of millibars. Configurations vary by rotor diameter and stand-off height to test the coupling between the ground-effect flow and the bed. The chamber pressure and temperature are continuously logged, the rotor speed (RPM) is measured, and the onset of motion is detected visually using a laser–camera setup aimed at the surface. Because raw RPM and images are not yet comparable, measurements are translated into friction velocity at the bed through two independent routes:

1. Through a combination of a rotorcraft scaling model based on wall-shear stress from Rabinovitch *et al.* (2021) and the actuator-disk approximation.
2. Through logarithmic Law-of-Wall calculation from measured near-bed flow using a representative roughness length.

These estimates are cross-checked against classical aeolian threshold formulations to place the results in established context.

The thesis has four principal outcomes:

1. **Feasibility and trend of thresholds across the tested range.** Lowering pressure raises the friction velocity required to initiate motion. The mechanism is straightforward: in thinner air, momentum flux to the surface decreases, so higher induced velocities are needed to deliver the same wall shear. In the smallest-rotor configuration at the lowest density reached, sustained saltation is not observed even at maximum RPM, indicating that the fluid threshold lies beyond that setup's operating envelope. Across accessible densities, thresholds determined via the law-of-the-wall rise nearly linearly with decreasing density and align reasonably with modern fluid-threshold models for the grains tested.
2. **Hysteresis between initiation and sustainment.** Once grains are mobilized, the system continues transporting material at lower shear than was required to start. This operationally important gap between initiation and continuation means that saltation can persist under conditions that would not have initiated motion from rest.
3. **Modelling sensitivity at low pressure.** Accurate treatment of kinematic viscosity is crucial. Analyses that keep the kinematic viscosity constant show growing bias as pressure falls, whereas varying it for different pressures, improves agreement between the two friction-velocity routes and classical thresholds. A persistent divergence remains between friction velocities obtained from the rotor–shear mapping and from the law-of-the-wall, with the rotor-based estimate running higher and the gap widening at lower density—evidence that simplified actuator-disk mappings under-resolve near-wall jet structure, tip-vortex effects, and swirl in thin air.

These results imply that scaling from Earth to Mars-analogue conditions cannot rely on density alone. Viscosity's pressure dependence must be included, differences between initiation and sustainment should inform operational margins, and hazard assessments should treat disk loading, hover height, and ground-effect structure as well. On the practical side, this means that the rotorcraft should carefully be designed to improve the safety of the flight.

This thesis does not test the very low pressure regime near true Martian ambient where some wind-tunnel studies suggest non-linear behaviour, therefore no claims are made for that range. Future work should extend experiments toward 6–10 mbar with higher-sensitivity velocimetry and top-down high-speed imaging to sharpen onset detection, incorporate gas composition effects (air versus CO_2), systematically vary grain size, density, moisture, and electrostatics, and tighten the link between measurement and prediction through higher-fidelity aerodynamic models. Continuing along these recommendations, can improve the scaling laws that mission planners can rely on when descending into the dust.

This page was intentionally left blank

Preface

This thesis is the result of my master's research on dust entrainment by rotor downwash across Earth–Mars pressure gradients, conducted as part of the MSc Aerospace Engineering program at TU Delft in collaboration with the Royal Netherlands Air Force (RNLAF).

Through this work, I was able to combine my passion for space exploration and engineering, bringing me a small step closer to what I have dreamed of since childhood: becoming an astronaut. I gained hands-on experience with hypobaric testing, aerodynamic modelling, and the practical challenges of running experiments under extreme conditions.

First, I would like to express my sincere gratitude to my supervisor, Sebastiaan, for his guidance, critical feedback, and continuous enthusiasm. The latter was especially important to me, as I have faced many personal challenges this year. I could not have done it without the motivation, space, and understanding you have given me. I also want to thank Johan and Alexander from the Flight Hall and Eric from the MAVLab for their assistance during the experimental phase. In addition, I am grateful to Patrick and Paul from Item Systems for their generosity and invaluable expertise during the design of the test box.

Furthermore, I would like to thank the CML team (Fred, Alicia, Liscia, Niels, Yuval, Peter, Dave, Simon, Erik) for their technical support and for making me feel welcome from day one. It was truly a pleasure to work alongside all of you, and I look forward to continuing this journey and crossing paths again in the future.

Last, but certainly not least, I am deeply grateful to my friends and family. 2025 has not been an easy year, and without the support I received from all of you, I would not have made it to the end. Mama, you have been both my punching bag and my greatest support throughout this journey. Jens, thank you for being there every single day and for making me laugh whenever I was crying. I also want to acknowledge the lifelong friends I have made during my studies: Siert (my greatest dining partner); Markus (for our endless tea breaks); Aïcha, Luis, and Mitchell for the unforgettable times as board members of Artemis; and Sahir, Ana, Nikolaus, and Nils, who made working throughout the summer and holidays surprisingly pleasant.

Thank you to my lifelong friends Tim, Maud, Marloes, and Basia, who, no matter how busy or far away they are, always check in on me and offer a shoulder to lean on. And lastly, I cannot forget Sander and Anita, who I consider family and let me cuddle with my favourite distraction: Yuki.

This project has been a life-changing experience, and I hope the work presented here will bring us one step closer to exploring the universe.

R.M. van der Voort
Rotterdam, October 2025

”You can’t always roll a six, but rolling a one four times in a row is just a bummer.”

Jens

Contents

Summary ii

Preface v

List of Figures x

List of Tables xi

Nomenclature xii

1 Introduction 1
- 1.1 Scope and Research Gap . . . 1
- 1.2 Research Question . . . 1
- 1.3 Thesis Outline . . . 2

2 Scientific Background 3
- 2.1 Dust Lofting Mechanism . . . 3
  - 2.1.1 Environmental Differences: Earth vs. Mars . . . 3
  - 2.1.2 Fundamentals of Dust Entrainment . . . 4
  - 2.1.3 Brownout . . . 6
  - 2.1.4 Non-linear Pressure Effects . . . 7
- 2.2 Rotorcraft Dynamics . . . 8
  - 2.2.1 Rotor Downwash and Ground Effect . . . 8
  - 2.2.2 Flow Structures: Tip Vortices and Wake Development . . . 9
  - 2.2.3 Rotor Performance vs. Air Density . . . 10
  - 2.2.4 Rotor Performance vs. Shear . . . 10
- 2.3 Models . . . 11
  - 2.3.1 Rabinovitch's model . . . 11
  - 2.3.2 Low Pressure Saltation Model . . . 12
  - 2.3.3 Ingenuity Flight Observations . . . 13
  - 2.3.4 Other Relevant Models and Frameworks . . . 13
  - 2.3.5 Comparison and Critical Analysis . . . 13
- 2.4 Experimental Test . . . 14
  - 2.4.1 Overview of Experimental Work on Dust Entrainment . . . 14
  - 2.4.2 Wind Tunnel and Hypobaric Studies . . . 15

3 Materials and Methods 16
- 3.1 Materials and Equipment . . . 16
  - 3.1.1 Hypobaric Chamber . . . 16
  - 3.1.2 Test Box . . . 17
  - 3.1.3 Rotor System . . . 18
  - 3.1.4 Sediment Material . . . 20
  - 3.1.5 Measurement Systems . . . 21
- 3.2 Experiments . . . 22
- 3.3 Data Analysis . . . 24

4 Results 26
- 4.1 Threshold Predictions by Shao and Kok Models . . . 26
- 4.2 Small Rotor Experiment at Height h_1 . . . 27
- 4.3 Small Rotor Experiment at Height h_2 . . . 29
- 4.4 Large Rotor Experiments . . . 31
- 4.5 Image Analysis of Sand Movement . . . 31

5 Discussion **33**
5.1 Viscosity 33
5.2 Grain Properties 34
5.3 Gravity 35
5.4 Atmosphere 35
5.5 Moisture 36
5.6 Comparison to Models 36
5.7 Rotorcraft performance 37
5.8 Thrust Estimation 38
5.9 Recommendations 39

6 Conclusion **40**

References **42**

A Models Comparison **46**

B Collected Data **49**

C Code: Shao & Lu, and Kok et al. **50**

D Code: Law of Wall **52**

E Code: Rabinovitch **53**

F Gantt Chart **57**

List of Figures

2.1 Forces and flow properties governing particle detachment by wind. In the boundary layer, lift (F_L) and drag (F_D) must overcome adhesion (F_{adh}) and weight (F_n), with shear stress defined by air density(de Vet *et al.*, 2014). 5
2.2 Threshold shear stress vs. pressure. (Andreotti *et al.*, 2021) 7
2.3 Rotor-induced ground flow pattern (Rabinovitch *et al.*, 2021). 9
2.4 Friction velocity vs helicopter altitude (Lemmon *et al.*, 2022) 11

3.1 The CML hypobaric chamber. The glass window through which the test box is visible is shown. 17
3.2 Control panel used to regulate chamber pressure via equivalent flight altitude. 17
3.3 Exploded view of the aluminium–plexiglass test box with main parts indicated. 18
3.4 Rotor setup in the test box with (a) the small propeller ($D = 0.35$ m) and (b) the large propeller ($D = 0.64$ m). Shown are the adjustable mounting rod, motor mount, control box, sandbed, laser & camera setup, and a LEGO Technic 30682 piece in the lower right corner for scale. 19
3.5 Schematic overview of the electrical architecture and data connections. 19
3.6 Remote control station for the rotor setup (outside the chamber) connected via fibre link to the in-chamber router. 20
3.7 Landscape of Soestduinen. 21
3.8 Quartz sand collection in Soestduinen. 21
3.9 Laser-diode and camera arrangement used for threshold detection via light-sheet imaging and motion analysis. 22
3.10 Anemometer. 22
3.11 Complete assembly of the setup in the hypobaric chamber. 24
3.12 View of the assembly with the laser on and lights off after a test run. 24

4.1 Threshold friction velocity vs. air density for 50 µm, 200 µm, and 500 µm grains, comparing Shao and Lu (2000) and Kok *et al.* (2012) models. 27
4.2 Calculated friction velocity u_* vs. air density for the small rotor at h_1, for 50, 200, and 500 µm grains using the Law of the Wall method. 28
4.3 Calculated friction velocity u_* vs. air density for the small rotor at h_1, for 200 µm grains, Rabinovitch method. 28
4.4 Calculated friction velocity (or u_*) vs. air density for small rotor at h_2, for 50, 200, 500 µm grains using the Law of Wall method. 29
4.5 Calculated friction velocity (or u_*) vs. air density for small rotor at h_2, for 200 µm grains. 29
4.6 Image before saltation at 720 mbar with small rotor h_1. 32
4.7 Image during saltation at 720 mbar with small rotor h_1. 32
4.8 Processed difference image, showing regions of sand motion (bright) at 720 mbar with small rotor h_1. 32
4.9 Circular patch forming. 32

5.1 Calculated friction velocity (or u_*) vs. air density for small rotor at h_1, for 200 µm grains, using the kinematic viscosity as a pressure dependent parameter. 34
5.2 Calculated friction velocity (or u_*) vs. air density for small rotor at h_1, for 200 µm grains, using Martian gravity. The deviation from the Rabinovitch model has increased, since this model is indepedent of gravity. 35
5.3 Calculated friction velocity (or u_*) vs. air density for small rotor at h_1, for 200 µm grains 37
5.4 Calculated friction velocity (or u_*) vs. air density for small rotor at h_2, for 200 µm grains, using Martian gravity 37

5.5 Calculated friction velocity u_* vs. RPM for small rotor at h_1, for 200 μm grains. A least-square fit provides a linear trend line: $u_* = 0.0007\omega - 0.7665$, with $R^2 = 0.9982$. 38

List of Tables

2.1 Comparative Atmospheric and Dust Properties: Earth vs. Mars. 6

3.1 Trade-off table for grain material. 21
3.2 Summary of rotor configurations and pressure sweep types. 23

4.1 Threshold conditions for saltation in the small rotor experiment at height h_1. Data are shown for multiple ambient air densities (in kg/m^3) and three grain sizes. For each condition, the near-bed wind speed $u(z{=}5\ \text{mm})$, the friction velocity from the Law of the Wall (u_*^{LoW}), the rotor pressure drop Δp, rotor thrust T, and the rotor speed at threshold (RPM) are given. Also shown is the friction velocity u_*^{Rab} estimated via the Rabinovitch method. 29
4.2 Threshold conditions for the small rotor at the higher altitude h_2. Columns are analogous to Table 4.1. The threshold friction velocities required are similar to those at h_1, but higher rotor RPMs were needed to achieve them due to the increased rotor height. 30
4.3 Raw threshold measurements for Test 1 (constant p). 31

A.1 Comparison of Dust Lofting and Saltation Models for Mars (part 1) 47
A.2 Comparison of Dust Lofting and Saltation Models for Mars (part 2) 48

B.1 Threshold friction velocity from Shao & Lu and Kok formulations for different particle diameters 49

Nomenclature

Abbreviations

Abbreviation	Definition
BLDC	Brushless DC Motor
CFD	Computational Fluid Dynamics
CML	Centre for Man and Aviation
CO_2	Carbon Dioxide
ESC	Electronic Speed Controller
IGE	In Ground Effect
LDA	Laser Doppler Anemometry
LiPo	Lithium-Polymer Battery
MARSWIT	Mars Surface Wind Tunnel
N_2	Nitrogen
NASA	National Aeronautics and Space Administration
O_2	Oxygen
OGE	Out of Ground Effect
OPC	Optical Particle Counter
PETG	Polyethylene Terephthalate Glycol
PISWERL	Portable In-Situ Wind ERosion Laboratory
PIV	Particle Image velocimetry
SRH	Sample Recovery Helicopter
RPM	Revolutions Per Minute
UAV	Unmanned Aerial Vehicle
UH	Utility Helicopter
UBEC	Universal Battery Eliminator Circuit

Symbols

Symbol	Definition	Unit
A	Rotor Disk Area	[m^2]
A_{ft}	Fluid-Threshold Coefficient (Kok)	[-]
A_{it}	Impact-Threshold Coefficient (Kok)	[-]
A_N	Threshold Coefficient (Shao–Lu)	[-]
a	Strain Rate	[s^{-1}]
C_f	Skin-Friction Coefficient	[-]
d	Particle Diameter	[m]
d_p	Representative Particle Diameter	[m]
D	Rotor Diameter	[m]
F	Dust Entrainment Flux	[$kg\,m^{-2}\,s^{-1}$]
F_{adh}	Adhesive/Cohesive Force	[N]
F_D	Aerodynamic Drag Force	[N]
F_L	Aerodynamic Lift Force	[N]
F_n	Normal Force (Weight)	[N]
g	Gravitational Acceleration	[$m\,s^{-2}$]
h	Rotor Height Above Bed	[m]
h_1	Lower Rotor Height (0.5D)	[m]

Symbol	Definition	Unit
h_2	Higher Rotor Height (1.0D)	[m]
m	Mass	[kg]
$\dot{m}$	Mass Flow Rate	[kg s^{-1}]
n	Dust-Flux Scaling Exponent	[-]
p	Static Pressure	[Pa]
R	Rotor Radius	[m]
r	Radial Distance from Axis	[m]
T	Temperature	[K]
T	Thrust	[N]
$u(z)$	Mean Wind Speed at Height z	[m s^{-1}]
u_*	Friction Velocity	[m s^{-1}]
u_{*t}	Threshold Friction Velocity	[m s^{-1}]
$u_{\max}$	Peak Outwash Velocity	[m s^{-1}]
v_0	Freestream Velocity	[m s^{-1}]
v_e	Exit Velocity	[m s^{-1}]
v_i	Induced Velocity in Hover	[m s^{-1}]
v_{vortex}	Vortex-Induced Velocity	[m s^{-1}]
v_{wake}	Wake Velocity	[m s^{-1}]
w	Mean Downwash Velocity	[m s^{-1}]
z	Height Above Surface	[m]
z_0	Aerodynamic Roughness Length	[m]
γ_{coh}	Cohesion Parameter (Shao–Lu)	[kg s^{-2}]
γ_{eff}	Entrainment Efficiency Coefficient (flux law)	[m^{-2} s^{2}]
η	Hiemenz Similarity Variable	[-]
κ	von Kármán Constant	[-]
μ	Dynamic Viscosity	[Pa s]
ν	Kinematic Viscosity	[m^{2} s^{-1}]
ϕ	Hiemenz Similarity Function	[-]
$\phi''(0)$	Hiemenz Wall-Slope Constant	[-]
ρ	Air Density	[kg m^{-3}]
ρ_f	Fluid Density (generic)	[kg m^{-3}]
ρ_p	Particle (Grain) Density	[kg m^{-3}]
σ	Rotor Solidity	[-]
τ	Shear Stress	[Pa]
τ_t	Threshold Shear Stress	[Pa]
τ_{wall}	Wall Shear Stress	[Pa]
Ω	Rotor Angular Speed	[rad s^{-1}]

1

Introduction

Rotorcraft operating near the ground can entrain dust and fine particles into the air through the intense airflow generated by their rotors (Wadcock *et al.*, 2008; Warmbrodt, 2025). On Earth, this phenomenon is known as helicopter brownout, which is described as a hazardous loss of visibility caused by a cloud of dust entrained into the air by rotor downwash during take-off or landing (NATO, 2012; Warmbrodt, 2025). Brownout has been a serious safety concern in military and civilian operations, as the swirling dust can severely reduce visibility and interfere with sensors, and damage equipment (NATO, 2012). On Mars, the interest in rotor-induced dust entrainment has grown with the success of the Ingenuity helicopter flight demonstrations and plans for future aerial vehicles (Fisher & Johnson, 2024; Logreira, 2023). A key question to answer is how the different atmospheric conditions on Mars (with a surface air density less than 1% of Earth) modulate the threshold and severity of dust lifting by a rotor downwash (Caprace *et al.*, 2024; Lemmon *et al.*, 2022; Rabinovitch *et al.*, 2021). Understanding this is not only critical for mission safety (*e.g.*, avoiding damage or contamination from Martian dust), but also interesting from a scientific point of view in understanding, as it ties into the broader physics of aeolian processes in different environments (Fisher & Johnson, 2024; Sullivan & Kok, 2017).

1.1. Scope and Research Gap

This thesis focusses on the threshold conditions and the intensity of dust entrainment caused by rotor downwash, comparing the behaviour across an Earth to Martian-like atmospheric pressure gradient. While rotorcraft brownout is well-studied at Earth's sea-level conditions (NATO, 2012; Warmbrodt, 2025), there is a lack of research covering the effects of a different environment, such as the thin Martian atmosphere. Previous studies have investigated wind-driven dust lifting on Earth and Mars separately (Bagnold, 1994; Iversen & White, 1982; Shao & Lu, 2000), and recent experiments have even revealed unexpected behaviours of sand and dust entrainment at low pressures, such as the reduction of the threshold shear velocity, which will be discussed further in this report (Andreotti *et al.*, 2021). However, the specific case of rotor downwash inducing dust lofting under reduced pressure remains poorly quantified (Caprace *et al.*, 2024; Rabinovitch *et al.*, 2021). In particular, it is not well known how much lower ambient pressure (and thus atmospheric density) alters the critical conditions (such as the minimal shear stress and friction velocity) required to lift dust from the ground, and how the amount of dust lofted scales with pressure (Lorenz, 2012). This gap is significant given upcoming applications: for example, future Mars missions (*e.g.* Mars Sample Return helicopters) or even rotorcraft for Titan will operate in atmospheres very different from Earth's, where the intuition from terrestrial helicopters may not directly apply (Logreira, 2023; NASA, 2019).

1.2. Research Question

In light of the above, the main research question of this thesis is:

”*How are the thresholds and the intensity of dust entrainment by rotor downwash modulated over an Earth to Martian-like pressure gradient?*”

In other words, this thesis aims to determine how a reduction in ambient pressure from Earth-normal levels to Mars-like levels influences (a) the minimum conditions needed to entrain dust from the surface, and (b) how the rotor's dynamics influence dust lofting rotor's downwash. This question covers several physical aspects: the effect of air density on aerodynamic shear stress (and thus the friction velocity at the ground, the role of atmospheric parameters and particle characteristics, and the changes in rotor airflow structure in thin air.

To support the main research question, the following sub-questions are addressed:

1. How does a reduction in ambient pressure affect the threshold shear stress and friction velocity required to initiate particle motion?
2. How does the amount and behaviour of entrained dust scale with atmospheric density?
3. How do rotor parameters (*e.g.*, thrust, RPM) influence entrainment at different pressures?
4. How do the experimental observations compare with existing theoretical and empirical models?

To address this question, the research combines experimental and theoretical approaches. A custom rotor test setup in a hypobaric chamber is used to directly observe dust lofting events at different pressures, while comparisons with existing models from literature are used to interpret the results. By experimenting in different pressure regimes from Earth ambient to approximations of Martian surface, the study captures a diverse gradient and aims to validate any predicted non-linear transitions in behaviour.

1.3. Thesis Outline

The thesis is organised into six chapters. In Chapter 1, the scope of the research is outlined, the knowledge gap is identified, and the main research question is formulated. In Chapter 2, the scientific background is presented, including the physics of dust entrainment, rotor downwash, and relevant theoretical models. Chapter 3 describes the experimental setup and methodology used to investigate dust entrainment under varying pressures. In Chapter 4, the results are presented, followed by a detailed analysis in Chapter 5, where findings are interpreted, compared with existing models, and discussed in the context of rotorcraft operation in low-pressure environments. Finally, Chapter 6 summarizes the main conclusions, highlights the contributions of the thesis, and provides recommendations for future research.

2

Scientific Background

This chapter provides the physical background for rotor-induced dust entrainment across Earth–to–Mars conditions. We first contrast the atmospheric and soil environments that govern entrainment (Section 2.1), then set the key scalars and thresholds (law of the wall, shear stress, friction velocity) and the roles of aerodynamic, gravitational, and cohesive forces. We next examine rotor downwash, ground effect, and wake structures that control near-surface shear (Section 2.2), and finally review analytical, experimental, and computational models relevant to Martian operations (Section 2.3). Together, these elements frame the assumptions and limits that are used for the experimental approach in Chapter 3.

2.1. Dust Lofting Mechanism

Understanding dust lofting by helicopter rotors requires a careful comparison of the different environmental conditions on Earth and Mars. The Martian surface has an extremely low atmospheric pressure and density, together with weaker gravity-factors that affect how aerodynamic forces interact with surface particles. Additionally, the composition and size distribution of surface dust vary significantly between the two planets, influencing both the initiation and behaviour of sediment transport. This section outlines the key atmospheric and soil differences that shape dust entrainment dynamics in each environment.

2.1.1. Environmental Differences: Earth vs. Mars

The Martian atmosphere is extremely thin and cold compared to Earth's (Williams, 2025). Surface pressure (p) on Mars averages only around 6 mbar, which is about 0.6% of Earth's sea-level pressure (Williams, 2025). The corresponding atmospheric density (ρ) is about 0.020 kg/m^3 (in the order of 1-2% of Earth's density). This indicates that the near-surface air on Mars is as thin as Earth's atmosphere is at about 35 km above the surface. According to the ideal gas law, lower pressure leads to lower density, which greatly weakens several aerodynamic forces for a given wind speed (Williams, 2025). Gravity (g) on Mars is also much lower, approximately 3.71 m/s^2, which is about 38% of Earth's gravity (9.81 m/s^2) (Williams, 2025). Gravity is independent of atmospheric state, therefore in lower gravity less force is needed to lift a particle off the ground, partially counteracting the effect of thin air. However, the reduced gravity also allows dust to stay suspended longer once lofted, potentially contributing to the dust hazes on Mars (Waza *et al.*, 2023).

A key difference between Earth and Mars lies in their surface dust properties. Martian regolith is made up of very fine dust (10-50 μm) composed largely of iron oxides and basaltic minerals like pyroxene and olivine (Perko *et al.*, 2002), with a particle density of about 2900-3300 kg/m^3 (Hamilton, 2010). Over 90% of airborne dust is 1-3 μm, while saltating grains can be up to 1000 μm (Sullivan *et al.*, 2008). Mars' thin, CO$_2$-rich atmosphere requires high wind speeds (20-30 m/s) to move sand-sized particles (Balme & Hagermann, 2006; Mahaffy *et al.*, 2015).

On Earth, mineral dust (quartz, feldspar, clay) has a particle density of 2600-2800 kg/m^3 (Hillel, 1998). Airborne dust is typically < 10 μm, while saltating grains are 100-500 μm (Southard, 2019). Earth's atmosphere (78% N_2, 21% O_2) allows saltation at much lower wind speeds (6-10 m/s) (NOAA, 2024).

These differences in dust composition, grain size, and atmospheric conditions lead to very different dust transport dynamics on the two planets.

2.1.2. Fundamentals of Dust Entrainment

Before examining rotor-induced dust lofting, it is essential to set the wind-flow scalars used below. A method to establish the shear stress from the wind velocity, is through the use of the Law-of-Wall. If wind speed *u(z)* is measured as a function of height *z* above the surface in the downwash region, it can be fit in a boundary-layer profile (Hébrard *et al.*, 2012; Kok *et al.*, 2012):

$$u(z) = \frac{u_*}{\kappa} \ln\left(\frac{z}{z_0}\right), \tag{2.1}$$

with von Kármán constant $\kappa \approx 0.4$ and roughness length z_0. The friction velocity u_* is related to the surface shear stress by

$$\tau = \rho_{air}\, u_*^2 \tag{2.2}$$

Entrainment refers to the process of particles leaving the surface and entering suspension or saltation due to aerodynamic forces (Wang *et al.*, 2023). The entrainment rate (F) of dust particles can be expressed quantitatively using:

$$F = \gamma\sqrt{\frac{\tau}{\rho_{air}}}\,(\tau - \tau_t) \tag{2.3}$$

where γ is an empirical efficiency parameter for dust entrainment, τ is the shear stress applied to the surface, ρ_{air} is the atmospheric density, and τ_t is the threshold shear stress for particle entrainment (J. Zhang *et al.*, 2022). This equation directly incorporates atmospheric density (ρ_{air}), which varies with atmospheric pressure, making it particularly relevant for understanding entrainment across different planetary environments.

Another key concept is the threshold friction velocity, often denoted u_{*t}. This threshold is defined as the minimum friction velocity (related to wind shear stress) at which particles on the surface begin to move (via rolling, sliding, or lifting) (Sweeney, 2022). In fluid mechanics terms, it corresponds to the point when the drag and lift forces from the wind on a particle overcome the resisting forces of gravity and cohesion holding the particle in place. At or above this threshold velocity, sediment transport initiates, and below it, particles remain stationary.

A widely used expression for the threshold friction velocity, accounting for both gravity and cohesion, is given by Shao and Lu (2000):

$$u_{*t} = A_N\sqrt{\frac{(\rho_p - \rho_{air})gd}{\rho_{air}} + \frac{\gamma}{\rho_{air} d}}, \tag{2.4}$$

where $A_N = 0.0123$, ρ_p is particle density, ρ_{air} is air density, g is gravitational acceleration, d is particle diameter, and $\gamma = 3 \times 10^{-4}$ kg/s^2 is the cohesion parameter.

Forces Governing Entrainment

Several forces determine whether a given particle will detach (i.e., be entrained):

- Aerodynamic drag and lift: As wind (or rotor downwash) flows over a particle, it exerts drag (parallel to the surface) and lift (normal to the surface). These aerodynamic forces scale with air density and the square of wind speed. Higher air density or velocity produces greater force on particles, promoting entrainment. In denser air (Earth), a lower wind speed is needed to achieve a given force than in thin air (Mars).
- Gravitational force: The weight of the particle, which equals its mass times gravitational acceleration, resists uplift. Heavier or larger particles (and higher gravity) raise the threshold velocity. Mars's lower gravity reduces the weight of particles, making it easier to lift a grain of given size compared to Earth (Williams, 2025).

- Cohesion and adhesion: Particles, especially fine dust, experience inter-particle cohesion. This arises from van der Waals molecular forces, electrostatic charges, and (on Earth) capillary forces if moisture is present (Balme & Hagermann, 2006). Cohesive forces ”bind” dust grains to each other and to the surface, creating an additional resistance that must be overcome. Cohesion is highly significant for grains in the dust size range (< 100 μm), causing a strong variability in threshold conditions. In fact, observations show that threshold friction velocity for very fine particles can vary greatly due to differences in cohesive contacts between grains. On Mars, the absence of water means van der Waals and electrostatic forces dominate cohesion, whereas on Earth, even a little moisture can largely increase cohesion (Shao & Klose, 2016).

All forces acting on the particles are visualised in Figure 2.1.

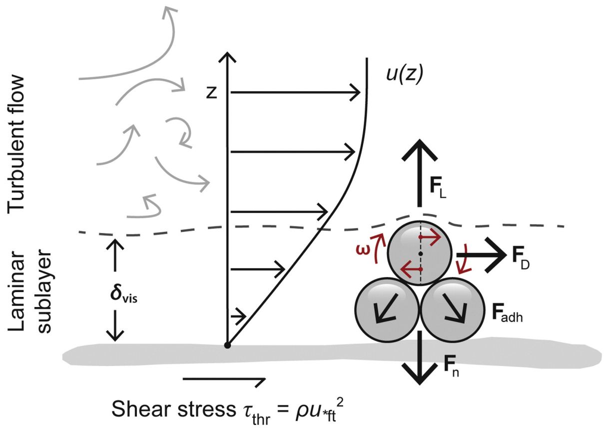

Figure 2.1: Forces and flow properties governing particle detachment by wind. In the boundary layer, lift (F_L) and drag (F_D) must overcome adhesion (F_{adh}) and weight (F_n), with shear stress defined by air density(de Vet *et al.*, 2014).

When wind shear stress on the surface becomes large enough to overcome gravity and cohesion, particles will start moving. Initially, larger sand grains (which have lower cohesion per mass) might move by rolling or hopping, and their impacts can help eject finer dust. This is known as saltation bombardment or sandblasting (Alfaro *et al.*, 2022). The threshold friction velocity needed to directly lift very fine dust by aerodynamic force alone is often higher than that for sand, so dust in natural dust storms is usually injected into the air by the impacts of saltating sand grains. Once some grains are mobilized, impacts and splashing transfer momentum to neighbouring grains, lowering the effective impact threshold and sustaining transport at mean shear below the initial fluid threshold. These effects are known as collective grain effects (Andreotti *et al.*, 2021).

Kok *et al.* (2012) derived an expression that both approximates the impact threshold friction velocity, as well as the fluid threshold friction velocity:

$$u_{*t} = A\sqrt{\frac{\rho_p - \rho_{air}}{\rho_{air}} gd} \tag{2.5}$$

where $A_{ft} = 0.10$ and $A_{it} = 0.082$.

Typical threshold friction velocities on Earth (at sea level) for loose sand are on the order of 0.2-0.3 m/s, whereas thresholds for silt or dust-sized particles can be higher (0.5 m/s or more) due to cohesion (Duan *et al.*, 2013; Li & Zhang, 2011). Field measurements in desert conditions found dust emission began at 0.35-0.4 m/s in a Gobi Desert site (Li & Zhang, 2011). On Mars, earlier theoretical estimates suggested a much higher threshold wind speed would be required to mobilize sand and dust (because of the thin air). Classic models predicted needing very strong winds (30 m/s at the surface) to initiate saltation on Mars, which was relatively high, knowing that Mars does have active dust storms and dust devils (Iversen & White, 1982). However, more recent research and experiments indicate the situation is more nuanced, as Martian dust lifting can occur at lower friction velocities than expected, partly due to the mitigating factors of lower gravity and collective grain effects (Andreotti *et al.*, 2021).

In summary, Mars has a low-pressure atmosphere that, via the ideal gas law, results in low density. It also has a low-gravity environment with highly cohesive fine dust, whereas Earth (at sea level) has high air density and pressure, higher gravity, and often less cohesive surface dust. These environmental differences should be taken into account when designing a rotorcraft, as the rotor downwash will interact differently with the ground on each planet. The fundamental mechanics of dust entrainment are caused by a combination of several forces: aerodynamic, gravity and cohesive forces. The threshold friction velocity provides useful insights, as rotorcraft operating in different atmospheres must produce a certain minimum shear stress on the ground to initiate dust lofting. In Table 2.1 an overview is presented of the atmospheric and dust properties of both Earth and Mars.

Table 2.1: Comparative Atmospheric and Dust Properties: Earth vs. Mars.

Parameter	**Earth (Sea Level)**	**Mars (Near Surface)**
Atmospheric Pressure	1013 mbar	6 mbar
Atmospheric Density	1.225 kg/m^3	0.020 kg/m^3
Gravitational Acceleration	9.81 m/s^2	3.71 m/s^2
Mean Surface Temperature	288 K	214 K
Average Particle Diameter	10-100 µm	1-3 µm
Atmospheric Composition	78% N_2, 21% O_2	95% CO_2, 3% N_2, 2% Ar
Dust Composition	Quartz, clay minerals	Basaltic, Fe-oxides
Characteristic Particle Density	2500 - 2800 kg/m^3	2900 - 3300 kg/m^3
Cohesion Mechanism	Capillary (humidity)	Electrostatic/van der Waals
u_{*t}	0.2-0.3 m/s	0.5-0.6 m/s

2.1.3. Brownout

When a rotorcraft takes off or lands in a dusty area on Earth, the rotor's airflow can stir up a cloud of dust. Pilots refer to this hazardous loss-of-visibility event as ”brownout”. Technically speaking, helicopter brownout is the phenomenon where sand and dust particles are swept up by the rotor downwash during low-altitude hover, takeoff, or landing, obscuring the pilot's view of the terrain. Essentially, the rotor acts like a giant fan blowing air downward. When that high-speed air hits the ground, it rushes outward along the surface (the outwash or wall jet) and picks up loose sediment if the winds are strong enough. The dust cloud can lead to disorientation, loss of ground reference, and has caused numerous accidents in military and civilian operations, making brownout a serious safety concern in Earth applications (Modesto, 2017). The strongest dust pickup occurs in an annular region near the rotor edge, where shear stresses peak (Caprace *et al.*, 2024; Phillips *et al.*, 2010; Wadcock *et al.*, 2008). Section 2.2 will dive deeper into the causes and effects of brownout due to the rotorcraft.

Dust Lifting under Martian Conditions

Ingenuity's 2021 flights on Mars confirmed that rotorcraft can loft dust under Martian conditions. Imagery from Perseverance showed visible plumes during takeoff and landing, validating pre-flight models of rotor-induced dust entrainment (Lemmon *et al.*, 2022; Ventura Diaz & Caprace, 2024). Despite the thin atmosphere, Mars's low gravity and fine surface particles enable efficient dust lifting, with observed friction velocity thresholds ($u_{*t} \approx 0.54$ m/s) comparable to Earth (Ventura Diaz & Caprace, 2024). Observational work also reports Earth-like sediment transport fluxes on Martian dunes during active conditions (Bridges *et al.*, 2012).

Recent modelling efforts have shown that Martian rotorcraft can mobilize dust effectively. Rabinovitch *et al.* (2021) found that the predicted and observed dust masses matched/overlapped with each other. High-fidelity simulations using vortex particle-mesh CFD methods reproduced dust lifting under Martian conditions when using threshold shear values (Caprace *et al.*, 2024; Ventura Diaz & Caprace, 2024). These models show shear peaks of 2.5-3 m/s under the rotor, which is above the threshold for dust entrainment.

Mars has shown that rotorcraft dust lifting is feasible. The lower gravity aids dust lofting, though generating sufficient wind requires more rotor power due to the thin air. While Martian dust clouds are more transient and localized than Earth's brownout events, Ingenuity's data has advanced understanding of rotorcraft-regolith interactions on other planets. This will also be discussed in more detail in Section 2.2.

2.1.4. Non-linear Pressure Effects

The transition from Earth's atmosphere to Mars's involves a pressure (and density) drop by about two orders of magnitude. Classic saltation models (valid at small Knudsen number with aerodynamic drag/lift balances) often assume smoothly varying, linear scaling of thresholds with density, as seen in Equation 2.2 (Bagnold, 1994; Iversen & White, 1982; Kok *et al.*, 2012). However, research indicates the relationship is highly non-linear, with distinct regimes of behaviour at different pressures (Andreotti *et al.*, 2021). This has important implications for performing scaled experiments and for operations in environments like high-altitude Earth- or simulated Mars conditions.

Scaling of Threshold with Air Density

As explained before, in classical models (*e.g.* Bagnold (1994) and Kok *et al.* (2012)), the threshold friction velocity u_{*t} for a given grain size is set by a balance of aerodynamic force and gravitational force, as shown in Equation 2.5. In the idealized case, lowering ρ_{air} would raise the threshold velocity by

$$u_{*t} \propto \frac{1}{\sqrt{\rho_{air}}}. \tag{2.6}$$

Mars's air density is 1/60 of Earth's, so this scaling suggests a $\sqrt{60} = 7.7$ increase in u_{*t}. However, this is partially offset by Mars's lower gravity g (and if grains are very small, cohesion would have a role). Even with a gravity adjustment ($g_{Mars} = 0.38 g_{Earth}$), it would still predict a significantly higher threshold wind speed on Mars than Earth for the same particle size. For many years, this led to predictions that only extremely strong winds (tens of m/s) could lift Martian dust, creating a "threshold paradox" when moderate winds were observed to drive dust entrainment (Andreotti *et al.*, 2021).

Laboratory and field experiments have shown that as pressure decreases into the Martian range, the behaviour enters a new regime. Recent wind-tunnel experiments by Andreotti *et al.* (2021) studied sediment transport from Earth-like pressures down to Mars-like and below, by using a vacuum chamber wind tunnel. They found that as the air pressure was lowered, the threshold wind speed did increase at first (consistent with classical models), but then unexpectedly dropped to a lower value in the Martian pressure range. In other words, the curve of threshold vs. air density is non-linear, which means that beyond a certain grain-to-air density ratio (4×10^5 as can be seen in Figure 2.2), the required wind speed for saltation initiation dropped.

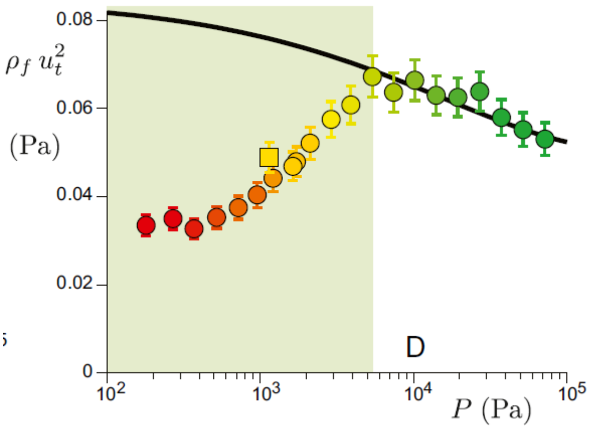

Figure 2.2: Threshold shear stress vs. pressure. (Andreotti *et al.*, 2021)

Mars conditions lie in this regime. The underlying cause may be that at low pressures the flow around particles is in a low-Reynolds-number regime and grain-grain interactions start to dominate initiation. Collective effects and grain inertia in the saltation layer become important: once dislodged, grains can transfer momentum efficiently to others with less aerodynamic damping, making it easier to sustain and even initiate motion than a single-grain aerodynamic model would predict. In addition, the reduced air pressure means less viscous damping, so grain impacts can splash others out more often. These findings possibly explain why Martian winds, though weaker, can drive Earth-like sediment transport fluxes (only about one order of magnitude lower than terrestrial deserts) (Andreotti *et al.*, 2021; Bridges *et al.*, 2012).

Implications for helicopters and Experiments

The non-linear pressure effect means that scaling rotor tests at sea level to Mars is not straightforward. Reduced-pressure testing and high-altitude environments allow the transition in entrainment behaviour to be observed. Experiments have measured cohesion parameters and thresholds on Mars-analogue soils under reduced pressure, noting that the absence of moisture and the gas composition can change cohesion (Perko *et al.*, 2002). At moderately reduced pressures, on the order of hundreds of mbar, the classic behaviour still holds and threshold increases as expected with thinner air. Hovering in ground effect can help raise near-wall shear. At Martian pressures, the threshold may not be as high as expected based on classical scaling, due to the regime described in Section 2.1.

In conclusion, atmospheric pressure has a large but complex influence on dust entrainment and brownout conditions for rotorcraft. From high-alpine terrestrial environments to the Martian surface, lower pressure affects the required threshold, the flow structures, and the efficiency of particle lifting in non-linear ways. For helicopter operations on Earth and for off-planet scenarios, this means the familiar brownout phenomena will act differently. By understanding the relationship between rotor downwash and dust lofting initiation, engineers can better predict when a helicopter will start kicking up dust and design mitigation.

2.2. Rotorcraft Dynamics

This section examines how rotor downwash interacts with the ground, with a focus on its aerodynamic structure and implications for surface shear and dust entrainment. It begins by introducing the physics of induced velocity in hover, then explores how proximity to the ground modifies flow patterns through the ground effect. The chapter also discusses how these effects vary with atmospheric density and rotorcraft design, providing the foundation for understanding dust lifting in different environments. These insights are critical for interpreting brownout on Earth and predicting rotor-induced dust dynamics on Mars.

2.2.1. Rotor Downwash and Ground Effect

When a rotorcraft hovers, its rotating blades accelerate air downward, generating a downward jet of air known as the rotor downwash. This downwash is essentially the reaction to the thrust produced by the rotor. By pushing air mass downward, the rotor experiences an upward lift force that supports the vehicle's weight. A simple momentum theory for a hovering rotor provides a useful relation between thrust (T), air density (ρ), rotor disk area (A), and the induced velocity through the rotor (v_i). In an ideal hover out of ground effect, the thrust is related to the mass flow and wake speed by:

$$T = \dot{m} V_{wake} \tag{2.7}$$

Assuming a uniform induced flow, $\dot{m} \approx \rho A v_i$ and $V_{wake} \approx 2v_i$ (Wadcock *et al.*, 2008). This leads to the classic result $T = 2\rho A v_i^2$, or rewritten as:

$$v_i = \sqrt{\frac{T}{2\rho A}} \tag{2.8}$$

Taking into account that $T = mg$ leads to the final equation of:

$$v_i = \sqrt{\frac{mg}{2\rho A}} \tag{2.9}$$

This induced velocity v_i represents the average downwash velocity through the rotor disk needed to generate thrust. The term T/A is often called the disk loading. The relation shows that a higher disk loading or a lower air density ρ requires a greater induced velocity v_i to produce the needed lift. For example, a heavy or small-rotor aircraft must expel air faster downward to hover, which can create stronger winds at the ground. A large rotor with the same thrust can hover with a lower downwash speed.

When the rotor operates close to the ground, the flow field changes due to ground effect. Ground effect refers to the influence of a solid surface in impeding the development of the rotor wake, which reduces the induced flow required for lift (Leishman, 2006). As the downward airflow hits the ground, it is redirected outward along the surface. This causes a buildup of pressure beneath the rotor and a reduction in the downward induced velocity compared to free-air hovering. The result is that a rotor hovering in ground effect (IGE), at altitudes within roughly one rotor diameter, needs less power and lower v_i for the same thrust than out of ground effect (OGE) (Filippone *et al.*, 2019; Yamauchi & Ramasamy, 2017).

In ground effect, the downwash pattern is not a simple tube but spreads radially when it reaches the ground. Downwash hits the ground plane and is deflected outward, creating a high-speed outward flow known as the ground jet or the outwash. A cylindrical wall jet expanding outward from just under the rotor to the surrounding environment can be seen through the outwash flow (Filippone *et al.*, 2019; Leishman, 2006; Yamauchi & Ramasamy, 2017). Even the tip vortex geometry is influenced by the ground. Rather than trailing far behind the aircraft, the tip vortices are compressed together and deflected outward along the ground. The outer parts of the rotor blades see the disturbed air of these vortices which are moved off centre. This decreases the self-induced turbulence that would otherwise be recirculated down into the rotor, improving rotor performance in ground effect (Filippone *et al.*, 2019; Yamauchi & Ramasamy, 2017). A schematic of a rotor hovering in ground effect with the downwash impacting the ground and spreading outward as a ground jet is shown in Figure 2.3.

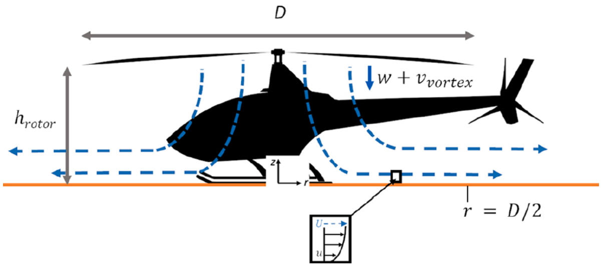

Figure 2.3: Rotor-induced ground flow pattern (Rabinovitch *et al.*, 2021).

As discussed in Section 2.1, rotor downwash near the ground can loft dust and debris, leading to hazards like brownout (Wadcock *et al.*, 2008). The intensity of this flow depends on the rotor thrust and disk loading. In hover, induced velocity increases as air density drops according to Equation 2.9.

2.2.2. Flow Structures: Tip Vortices and Wake Development

The rotor wake consists of trailing tip vortices shed by each blade due to the pressure difference between the upper and lower surfaces. In steady hover out of ground effect, these vortices form concentric helical sheets that convect downward and dissipate in the far wake (Wolf *et al.*, 2022).

When close to the ground, rotor downwash interacts with the surface to form distinct structures. One prominent feature is the ground vortex. This is a ring-shaped horizontal vortex formed at the edge of the outwash where it shears against the ambient air. This vortex moves outward and forms the boundary of disturbed flow (Phillips & Brown, 2008). In some conditions, part of the outward flow curls back up into the rotor disk. This recirculation creates an upflow near the rotor hub, sometimes called a fountain effect, as shown in experiments and CFD for the UH-60 (Wadcock *et al.*, 2008). Tip vortices can cause localized bursts of swirling air when they contact the ground. However, most dust entrainment is driven by the wall jet instead of individual vortices.

In Martian conditions, the Ingenuity helicopter provided a real-world example of rotor wake behaviour. During Ingenuity's flights on Mars, dust was lifted even when the vehicle was several meters high. This suggests that the rotor wake and its vortices were still interacting with the ground indirectly through persistent vortical structures. The coaxial design reduces net swirl but does not exclude persistent vortex structures (Lemmon *et al.*, 2022).

To conclude this section, a rotor in ground effect produces a characteristic flow pattern. A downward jet turns into a radial wall jet along the ground, bounded by a rolling ground vortex at the leading edge.

Tip vortices are forced to spread outward, and in some cases recirculating flows or vortex ring states can occur near the rotor or near the ground. Each of these flow features contributes to the spatial distribution of shear stress on the surface, which directly impacts dust entrainment. The next section discusses how changes in air density affect the rotor's ability to generate these flows.

2.2.3. Rotor Performance vs. Air Density

Air density is a crucial factor in rotorcraft performance. Lower density, as encountered at high terrestrial altitudes or on Mars, makes it harder for rotors to produce lift because there is less mass of air available for the rotor to push against per unit volume. For a rotor to generate a given thrust T in thinner air, it must accelerate the air to a higher velocity. As introduced earlier, Equation 2.9 indicates that if ρ decreases, v_i must increase. This relationship means that rotor downwash velocities scale inversely with the square root of air density for constant thrust and rotor area. Also, the required disk loading T/A rises relative to ambient pressure to achieve lift.

Rotational Speed

One direct consequence is on the required rotor rotational speed or blade pitch in thin atmospheres. On Earth, small helicopters can hover at a few thousand RPM with modest blade pitch. On Mars, Ingenuity compensated for the much lower density with counter-rotating rotors of large diameter and high RPM. The large rotor area and high blade velocity mitigate the low atmospheric density. In contrast, the same rotor in Earth's atmosphere could produce lift at a much lower RPM. Thus, as air density drops, either rotor area or rotor RPM, or both, must increase to maintain thrust. High altitude helicopters on Earth show a similar trend. Pilots must pull more power, with higher blade pitch and RPM, to hover at high density altitude, and eventually a ceiling is reached (Koning & Dominguez, 2024).

Reynolds Number

The change in air density also influences the rotor wake structure and blade aerodynamics. At lower atmospheric density, for a given rotor speed, the Reynolds number of the flow over the blades is lower. Ingenuity's blades, for instance, operate at Reynolds numbers on the order of 10^4 in Martian hover, which is an extremely low Reynolds regime for an aerospace vehicle (Koning & Dominguez, 2024). Airfoils at such low Reynolds number can have significantly lower lift coefficients and different stall characteristics than at the 10^5-10^6 range typical for helicopters on Earth. This means the blades are less efficient in thin air, requiring careful design, such as cambered airfoils, high tip speeds, and sufficient rigidity to avoid stall. The low density also means the rotor wake expands more. There is less ambient pressure to contain it, so the same pressure drop creates a larger volume flow. In other words, the rotor must sweep a larger volume of air per second to generate thrust in low density, which can lead to a more diffuse but fast-moving downwash (Koning & Dominguez, 2024).

It is important to consider gravity when comparing Earth and Mars. For a given mass, weight on Mars is about 0.38 of Earth, which reduces T and partly compensates for the low density requirement, although not fully. Using $v_i \propto \sqrt{T/\rho}$, the Martian required induced speed can still be a factor of several higher than on Earth. Increasing rotor area lowers the required induced speed. Ingenuity has an oversized rotor for its mass and still needs high RPM to fly (Koning & Dominguez, 2024).

Overall, in a lower atmospheric pressure and density, a rotorcraft needs higher rotor speeds and greater induced velocities to achieve a given lift. This leads to stronger downwash and outwash flows at comparable heights. The thin atmosphere shifts the operating point, which in turn influences how the rotor airflow interacts with the ground and entrains dust.

2.2.4. Rotor Performance vs. Shear

To quantify the shear produced by a rotor, equations for a turbulent wall jet can be used. The peak outwash velocity $u_{\max}$ might be known from experiments or momentum theory (Wadcock *et al.*, 2008), and then the shear stress is defined as:

$$\tau = \frac{1}{2} C_f \rho u^2 \tag{2.10}$$

where C_f is a friction coefficient depending on surface roughness. Many studies measure dust emission versus an integrated parameter (such as disk loading). Field tests in desert conditions compared dust concentrations generated by different helicopters. Disk loading emerged as a key parameter.

Helicopters with higher disk loading tended to produce more intense dust plumes (Gillies *et al.*, 2010):

$$\text{Dust Flux} \propto \left(\frac{T}{A}\right)^n, \quad n \sim 1\text{–}2 \tag{2.11}$$

This comparison assumes broadly similar operating states. RPM differences and control settings also modify unsteadiness and peak shear.

The distribution of shear stress under the rotor means the initial locus of particle lifting is a ring or annulus on the ground. Dust is then entrained into the outward flow. As it moves outward, it can form an expanding dust cloud or dust ring around the aircraft. If the rotorcraft stays in hover, this dust cloud may expand and be drawn upward around the vehicle. If the aircraft translates, the dust may trail behind or to the sides. Observations with Mars flight imagery indicate that dust can be raised outward of the vehicle footprint, consistent with peak friction velocity occurring around one to one-and-a-half rotor radii (Caprace *et al.*, 2024; Lemmon *et al.*, 2022).

2.3. Models

This section explores analytical and experimental models developed to predict dust entrainment by rotorcraft on Mars, with a focus on brownout-like effects caused by rotor downwash. It begins with an analytical framework by Rabinovitch for estimating surface shear stress under Martian conditions, then discusses laboratory-based low-pressure saltation experiments that reveal new threshold behaviours. The chapter also integrates real-world flight data from Ingenuity to validate and challenge these models, and highlights contributions from other frameworks such as CFD simulations and classical threshold theories. Together, these approaches form a baseline picture of how rotor-induced dust lifting behaves in Mars's thin atmosphere.

2.3.1. Rabinovitch's model

Rabinovitch *et al.* (2021) proposed a simplified scaling model to predict sediment mobilization beneath rotorcraft on Earth, Mars, and Titan. The model combines classic saltation threshold theory (see Section 2.1, Equation 2.4 and Equation 2.5) with a laminar stagnation-point (Hiemenz) approximation of the rotor wake, enhanced by an empirical treatment of tip-vortex effects (Rabinovitch *et al.*, 2021). Its aim is to provide a first-order estimate of whether dust or sand-sized particles are mobilized when a rotorcraft hovers close to the surface. The Rabinovitch model's main output is the peak friction velocity (u_*, via $\tau = \rho v^2$) that the rotor downwash can produce on the ground as a function of the rotor height. A higher friction velocity implies greater capability to lift and sustain particles. The model's predictions for Mars indicated that close to the ground, the rotor wash generates high shear stresses that can exceed typical dust entrainment thresholds, but these stresses decay rapidly as the rotorcraft ascends. Figure 2.4 illustrates the modelled decrease in friction velocity with increasing rotor height, based on Rabinovitch *et al.* (2021)'s formulation.

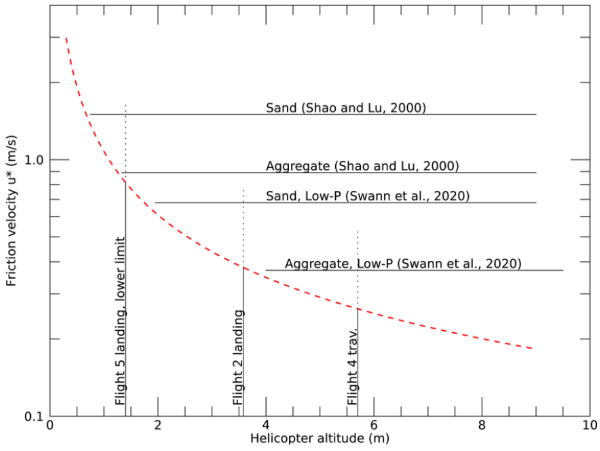

Figure 2.4: Friction velocity vs helicopter altitude (Lemmon *et al.*, 2022)

In this example, the model (red dashed curve) is plotted for a Mars-like atmospheric density of 0.02 kg/m^3 with Ingenuity's rotor parameters, whereas the horizontal lines refer to threshold friction velocities for sediment movement under Mars conditions. The conventional threshold (from an Earth-based model by Shao and Lu (2000)) is higher, while a low pressure threshold (from Swann *et al.* (2020)) is lower, reflecting differing expectations for how easily grains can be mobilized on Mars. As shown, the rotor-induced friction velocity u_* is high near the ground and falls off with height, crossing these threshold lines at certain altitudes.

The starting point is the definition of the threshold friction velocity for sediment entrainment (cf. Section 2.1):

$$u_{*t} = \sqrt{\frac{\tau_t}{\rho}} \tag{2.12}$$

The rotor wake is then approximated by an axisymmetric stagnation-point flow (classical Hiemenz solution) (Rabinovitch *et al.*, 2021). The governing similarity solution is:

$$\phi''' + 2\phi\phi'' - (\phi')^2 + 1 = 0, \tag{2.13}$$

with similarity variable $\eta = \sqrt{\frac{a}{\nu}}z$, where a is the strain rate and ν the kinematic viscosity. With boundary conditions $\phi(0) = 0$, $\phi'(0) = 0$, $\phi'(\infty) = 1$, the wall shear becomes

$$\tau_{wall} = \mu r\, a^{3/2}\nu^{-1/2}\phi''(0), \tag{2.14}$$

with $\phi''(0) \approx 1.31$.

The strain rate a depends on the jet velocity w. The mean downwash velocity (consistent with momentum theory; see Equation 2.9) is

$$w = 2\sqrt{\frac{T}{2\rho A}}, \tag{2.15}$$

with $T \simeq mg$ and $A = \pi R^2$. To account for tip vortices, an empirical vortex-induced velocity v_{vortex} augments a:

$$a = \frac{w + v_{vortex}}{2h_{rotor}}, \qquad v_{vortex} = \frac{2.3}{0.1\pi}\,\frac{T}{\sigma\rho A\Omega D}. \tag{2.16}$$

Combining gives

$$\tau_{wall} = \mu r \left(\frac{w + \frac{5.75}{\pi}\frac{w^2}{\Omega R\sigma}}{2h_{rotor}}\right)^{3/2} \nu^{-1/2}\phi''(0). \tag{2.17}$$

In summary, this model provides a tractable analytical framework for evaluating the severity of sediment mobilization beneath rotorcraft. While it cannot capture the full complexity of brownout dynamics, it offers a valuable first-order tool for assessing whether planetary rotorcraft such as *Ingenuity* or *Dragonfly* are likely to mobilize sediment during takeoff and landing.

2.3.2. Low Pressure Saltation Model

Andreotti *et al.* (2021) investigated sediment transport under Martian-like low pressure conditions and revealed a new regime for wind-driven saltation. This work combined laboratory wind tunnel experiments with analysis to challenge existing entrainment theories at very low atmospheric pressures. Andreotti *et al.* (2021) performed tests in a vacuum wind tunnel, gradually reducing air pressure to Martian levels (6-10 mbar), while observing when sand grains begin to move. The key finding was that the threshold wind speed required to initiate saltation on Mars is much lower than predicted by previous models once the air density drops below a certain point. Under Earth conditions, traditional models (which balance aerodynamic drag/lift against gravity and cohesion) can reasonably predict the threshold. However, at Martian atmospheric density (gas density 1% of Earth's and grain-to-air density ratios exceeding $4 \cdot 10^5$), the observed threshold wind speed is much lower than expected. This means that older models become inaccurate in the Mars density regime; they overestimate the wind or shear needed to start particle motion. This section directly links to the updated threshold perspective introduced in Section 2.1.

This unexpected reduction in threshold at extremely low pressure is due to a difference in the transport mechanism. Andreotti *et al.* (2021) suggest that when the fluid (air) is very thin, once a few grains are lifted, the grains can travel further and hit the surface with enough energy to eject other grains, initiating an increasing effect of dust lofting. Grain inertia in the collisional layer (also known as the saltation cloud) has a bigger role than the aerodynamic forces in the dust transport. Mars has a high grain to fluid inertia regime, where multiple effects among moving grains enable continuing saltation at lower wind stress than a single-grain threshold would imply. This is consistent with the concept of fluid and impact thresholds: the fluid threshold (to initiate motion) may be high, but the impact threshold (to sustain motion via grain impacts) is much lower. At Martian pressures, the gap between these thresholds seems smaller, or even new mechanisms lower the effective start threshold. They also observed that impact ripples formed in the sand with similar wavelengths and propagation speeds across the entire pressure range. This indicates that once saltation initiated, the resultant transport and ripple-forming process were surprisingly insensitive to air pressure, backing up the idea that grain inertia and impacts dominated over fluid drag in that regime.

2.3.3. Ingenuity Flight Observations

While the above models were developed theoretically or in laboratories, the flights of the Ingenuity Mars rotorcraft provided the first real-world dataset on rotor-induced dust entrainment in the Martian environment. Lemmon *et al.* (2022) analyzed high-speed video footage captured by the Perseverance rover to quantify dust lifting during Ingenuity's operations. By processing six flight videos, the researchers measured the size, movement, and mass of dust clouds kicked up by the rotorcraft's rotor downwash and correlated these observations with the rotorcraft's altitude and motion. One outcome was a threshold estimate of $u_* \sim 0.4$-0.6 m/s for dust lifting during landing phases (Lemmon *et al.*, 2022; Ventura Diaz & Caprace, 2024).

2.3.4. Other Relevant Models and Frameworks

Next to the specific studies described above, other models contribute to understanding dust entrainment under Earth and Mars conditions. These include classical wind erosion thresholds, newer low pressure threshold formulations, and computational fluid dynamics (CFD) simulations of rotorcraft dust lifting.

Classical Threshold Models (Earth-based)

A well-known concept in aeolian research is the threshold friction velocity u_{*t} (*e.g.*, Iversen and White (1982); see also Section 2.1). The Shao and Lu (2000) expression in Equation 2.4 remains a useful baseline, while Mars applications require adapted inputs accounting for low density and gravity.

Low Pressure Threshold Models

Swann *et al.* (2020) adjusted threshold criteria for Mars using wind-tunnel experiments at 6-10 mbar, finding lower thresholds than earlier Earth-based scalings suggested. Reported threshold shear velocities around 0.6-0.8 m/s for 150-200 µm grains align with Andreotti *et al.* (2021) and provide input parameters for rotor-induced erosion models (*e.g.*, Lemmon *et al.* (2022)).

CFD and Simulation Models

Computational fluid dynamics (CFD) models couple rotor aerodynamics with erosion algorithms to predict wall shear distributions and dust fluxes. Caprace *et al.* (2024) reproduced dust lifting signatures consistent with Ingenuity, and suggested a slower decay of wall shear with altitude than simple scaling would indicate-consistent with observed dust at 5-6 m.

2.3.5. Comparison and Critical Analysis

Comparing all the models and observations, several key points come to light. Atmospheric pressure plays a big role in dust entrainment, but not all models take it similar into account. Some, like Rabinovitch *et al.* (2021), include atmospheric density explicitly and apply across planets. Others, like the more classical threshold models, were built for Earth and require later adaptation. Recent work (*e.g.*, Andreotti *et al.* (2021)) shows that threshold wind speeds scale non-linearly with pressure, which is a crucial improvement.

A clear strength of the Rabinovitch model is that it correctly predicted Ingenuity's dust lifting at low altitudes (3 m), which is consistent with observations and low pressure threshold models like those of

Andreotti and Swann. However, it underestimates dust lifting at higher altitudes, where CFD results from Caprace *et al.* (2024) show shear stress persists longer than Rabinovitch's model suggests. This highlights the model's limitations in capturing unsteady effects and OGE behaviour.

The models also differ in the assumptions about how dust is lifted. Rabinovitch uses a friction velocity threshold as a trigger without specifying mechanisms, while Andreotti *et al.* (2021) studies suggest dust aggregates can break up and mobilize more easily than Earth-based models assume. This hints back to the underrepresented effects like cohesion and aggregate fragility, which are likely different under Martian conditions.

Validation remains limited. While some models align with observations (*e.g.*, Rabinovitch qualitatively, Andreotti quantitatively), most lack extensive *in-situ* data. Ingenuity's observed dust plumes provide valuable constraints, but only under one set of conditions. Future missions like the Mars Sample Recovery helicopter or Titan's Dragonfly could offer broader datasets for testing and refinement.

In conclusion, each model contributes useful insights, but none alone is sufficient. Table A.1 and Table A.2 include a summary of the models discussed, highlighting their origin, intended application, key parameters/outputs, assumptions, and any known validation status or discrepancies.

2.4. Experimental Test

This section examines how rotor downwash lifts dust under conditions ranging from Earth's atmosphere to Martian pressure. It begins with a review of prior experimental work in both terrestrial and Mars-analogue environments. Subsequent sections cover wind tunnel and hypobaric (reduced-pressure) studies, key measurement parameters, and sensor techniques. The chapter concludes by outlining the proposed experimental setup and its role in addressing current knowledge gaps relevant to planetary rotorcraft operations.

2.4.1. Overview of Experimental Work on Dust Entrainment

Dust entrainment by airflow has been studied in both Earth and Mars analogue environments. Full-scale field tests, scaled model experiments, and computational simulations have all been used to characterize how rotor vortices pick up soil particles. For example, NASA Ames researchers performed tests with rotorcraft hovering over prepared surfaces: by applying hundreds of small tufts on the ground and on a rotorcraft model, they visualized flow directions of the downwash and identified recirculating flow patterns that contribute to dust uplift (Wadcock *et al.*, 2008). Small-scale lab experiments have also been done with model rotors and even techniques like oil droplets on the ground to map out shear stress footprints (Y. Zhang *et al.*, 2017). These Earth-based studies established baseline knowledge on how rotorcraft generate near-ground turbulence and what parameters (rotor thrust, height above ground, soil type, etc.) influence the onset of dust lifting.

Starting in the 1970s-1990s, researchers used specialized wind tunnels to simulate Martian surface conditions. Classic experiments by Iversen and White (1982) and B. R. White *et al.* (1991) at NASA Ames' Mars Surface Wind Tunnel (MARSWIT) suggested very high winds would be required to initiate sand movement at Mars pressures. More recent experiments and rover observations have shown that Martian dust can be mobilized at lower wind stresses than previously believed, as discussed in Section 2.3. Andreotti *et al.* (2021) conducted low pressure wind tunnel experiments in a closed-circuit facility placed inside a vacuum chamber, exploring conditions down to Martian pressure (6-10 mbar). A major validation came from Lemmon *et al.* (2022). Videos of Ingenuity showed dust being lifted from 1.4-3.6 m altitude, and analysis estimated 1-2 g of dust mobilized per flight-far more (per unit mass) than on Earth. These results aligned with Rabinovitch *et al.* (2021) pre-flight models and helped validate high-fidelity CFD simulation.

Overall, Earth-based rotorcraft tests provided information on the role of vortices and shear flows in lifting particles, whereas Mars analogue studies showed that low pressure conditions affect the threshold and amount of dust that can be lifted. These findings highlight the importance of designing experiments at appropriate scales and conditions to capture the correct physics and reveal gaps: there is still no dataset from controlled lab experiments that spans the continuum from Earth pressure to Mars pressure for rotor outwash. This motivates the experimental approach outlined here.

2.4.2. Wind Tunnel and Hypobaric Studies

Simulating Martian dust entrainment in a laboratory requires recreating key aspects of the Martian environment, especially the low atmospheric pressure and low air density. Over the years, researchers have developed wind tunnel and hypobaric chamber experiments to investigate dust lifting under such conditions.

Wind Tunnels under Martian Conditions

One common approach is to use a vacuum chamber housing a wind tunnel. In these setups, the pressure inside the chamber can be reduced to Mars-like levels (on the order of 6-10 mbar), and then a flow of gas (often air or CO_2) is driven over a bed of soil or dust sample. For example, the wind tunnel experiments by Andreotti *et al.* (2021) employed a closed-loop (recirculating) wind tunnel inside a large vacuum chamber. This design allowed the pressure to be steadily lowered while maintaining flow over sand grains, making it possible to directly observe the onset of particle motion as a function of pressure. In such systems, gas composition and temperature can sometimes also be adjusted.

Challenges in Hypobaric Wind Studies

Conducting wind experiments at Mars-like pressure presents several technical challenges. First, achieving high wind speeds in thin air requires powerful fans or pressure differentials. Because air density is very low, a fan must reach high RPM to generate enough wind speed, as discussed in Section 2.2. Generating and accurately measuring such high speeds in a low-density environment is non-trivial. Second, scale effects and similarity laws are an issue. True Martian conditions are not just low pressure, but also lower gravity (0.38 g). Gravity affects particle weight and thus threshold. Altering gravity is not trivial; parabolic flight experiments indicate that reduced gravity further lowers the wind needed for saltation initiation, consistent with theoretical expectations. Aside from gravity, matching parameters like Reynolds number or Shields parameter between lab conditions and Martian conditions is complex. Researchers often choose between parameters (*e.g.*, using smaller grains or different gas densities) to approximate the same ratio of particle inertia to fluid forces. Another challenge is maintaining experimental integrity with dust under low pressure. Fine dust particles can adhere to surfaces due to electrostatic forces, which become relatively more significant in thin, dry atmospheres. Testing with dust in a vacuum system increases the risk of contaminating pumps and valves. Many hypobaric wind tunnel studies focus on sand-sized particles instead of very fine dust to avoid clogging filters or damaging vacuum pumps Van Leeuwen *et al.* (2021). Those that do use dust add traps or filters to capture particles before they reach the pumping system.

3

Materials and Methods

Based on the hypotheses developed in Section 2.3 and the identified measurement needs in Section 2.4, these experiments were designed to investigate how variations in air density influence rotor-induced dust entrainment.

The experimental tests aim to quantify the influence of air density on dust entrainment induced by rotor downwash, replicating Earth-to-Mars pressure gradients under controlled laboratory conditions. To achieve this, a fully operational rotor test rig had to be realised inside the hypobaric chamber at the Center for Man and Aviation (CML). Several practical and scientific challenges had to be overcome:

1. Establishing a stable connection between the rotor setup and the chamber's limited power feedthroughs.
2. Preventing dust from spreading through the chamber or damaging the vacuum pumps.

To address these issues, a modular and enclosed system was designed consisting of an aluminium-plexiglass test box, a single-rotor propulsion unit, and measurement and data acquisition instruments. The design allowed the study of near-surface aerodynamic shear and threshold dust entrainment in a safe, repeatable, and observable manner. The following sections describe each subsystem and the experimental procedures in detail.

3.1. Materials and Equipment

This section describes the materials, instruments, and facilities used to conduct the experiments. It covers the hypobaric chamber used to create low-pressure conditions, the rotor system and its electronics, the dust simulant material and its preparation, as well as the measurement instruments and data acquisition setup. Each subsection below describes the components and their specifications, providing the groundwork for the experimental methodology.

3.1.1. Hypobaric Chamber

The experiments were carried out in a hypobaric chamber located at the Center for Man and Aviation (CML), which is capable of simulating high-altitude/low-pressure environments. The chamber is a steel cylindrical caisson originally designed in the 1950s, with an inner volume of approximately 50 m^3 (length 5.4 m, diameter 2.9 m). It can reach pressures as low as 79 mbar (equivalent to about 56 000 ft), well below standard atmospheric pressure. The chamber is equipped with vacuum pumps and control systems to reduce and regulate the internal air pressure, as well as safety valves to prevent over-depression and enable rapid re-pressurisation if needed. Two access doors (an outer door and antechamber lock) provide entry, sealing against O-rings that ensure an airtight closure when depressurising the chamber (down to 79 mbar). For safety with human experiments, the chamber is fitted with an oxygen supply system and audio/video monitoring; since the present experiments were unmanned, only the camera was used.

For these tests, the entire experimental setup was placed inside the hypobaric chamber, in front of one of the glass windows. The chamber was used to conduct rotor-entrainment experiments at reduced pressures. Although these pressures are higher than the actual Martian surface pressure, they allow investigation of the underlying scaling behaviour in a lower-density regime, providing relevant physical insights for extrapolation to Martian conditions. The pressure was monitored via built-in sensors and a separate reference pressure gauge that was visualised through one of the internal cameras. From a separate control panel outside the chamber, a certified operator adjusted the ”flown height” (an operational parameter corresponding to an equivalent flight altitude, which is converted to atmospheric pressure using standard atmosphere calculations) to regulate the chamber pressure. The chamber was depressurized at rates set by the operator (slow to relatively fast, up to 6000 ft/min). It was later discovered that the chosen rate affected chamber conditions, this is discussed in Chapter 5. All information regarding the hypobaric chamber has been communicated through personal communication with 1Lt. Romeijn. The glass window through which the box is visible is shown in Figure 3.1, and the control panel in Figure 3.2.

Figure 3.1: The CML hypobaric chamber. The glass window through which the test box is visible is shown.

Figure 3.2: Control panel used to regulate chamber pressure via equivalent flight altitude.

3.1.2. Test Box

Inside the hypobaric chamber, a custom-build test box was used to prevent the sand grains from spreading through the chamber due to the exerted wind force by the rotor system. The primary purpose of this box was to keep the particles confined to a known area and to protect both the chamber’s vacuum pumps and instrumentation from contamination. The transparent walls enabled visual observation from outside the chamber. The rotor system was mounted on a vertical profile in the middle of the box, oriented to blow downward toward the floor; the rotor-arm height could be adjusted between runs. As the rotor blew downward, sand at the floor could be set in motion and circulate within the box, while the walls and lid contained the particles. The box was not airtight; a small vent near the top plate allowed pressure equilibrium with the chamber during pump-down.

The box is a rectangular frame made of aluminium profiles with transparent plexiglass (PET-G) panels on all sides. The inner dimensions are 1.0 m × 1.0 m base and 0.75 m height, providing a contained volume for the experiments. The frame was constructed from 40 mm × 40 mm aluminium profiles, joined with corner brackets and seals, to ensure rigidity and limit leakage. Clear 4 mm plexiglass sheets were mounted on each side, offering visibility and optical access. A rubber gasket (seal strip) lines panel edges to reduce gaps, making the box nearly dust-tight. The top plate was removable to allow access for adding/removing sand and adjusting equipment. An exploded view showing the main parts is provided in Figure 3.3.

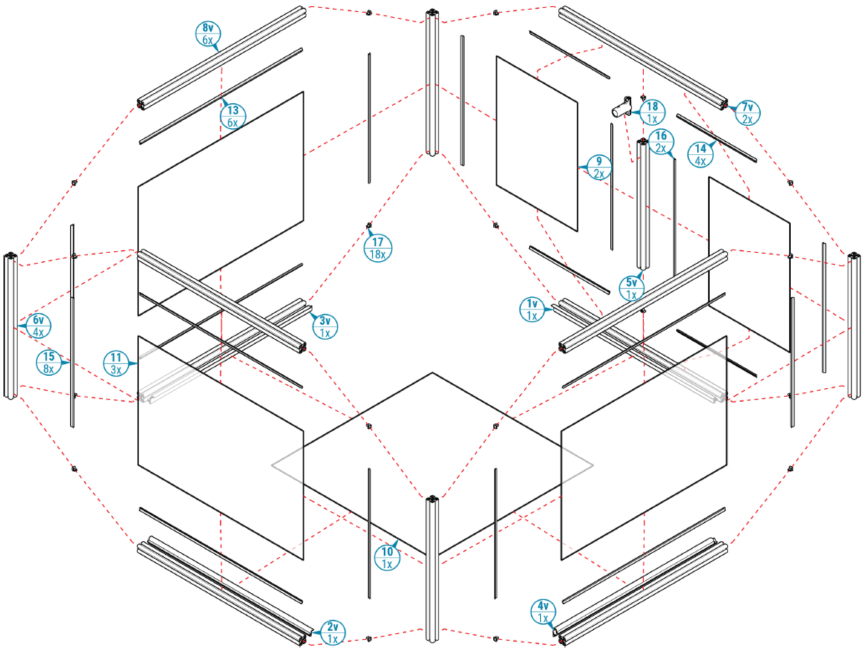

Figure 3.3: Exploded view of the aluminium–plexiglass test box with main parts indicated.

3.1.3. Rotor System

The rotor was a small-scale, single-rotor test rig designed to generate a controllable downwash over a granular bed inside the hypobaric chamber. The configuration resembled a hovering UAV; the rotor height could be manually adjusted for each test run. The system consisted of a fixed-pitch propeller driven by a brushless DC (BLDC) motor via an electronic speed controller (ESC), with onboard power and a flight controller for repeatable throttle commands and logging. The original rotor setup was previously built by Ing. van der Horst (TU Delft) and was adapted in collaboration with him.

Propellers

Two sets of two-bladed, fixed-pitch propellers were used. These correspond to two rotor diameters and were selected to isolate how rotor size influences near-surface shear and threshold conditions, and the sensitivity of the rotorcraft parameters in the Rabinovitch model. The primary rotor (Tarot) had a diameter of $D = 0.35$ m and is typical for a small UAV rotor; the blade pitch was fixed and thrust was modulated via RPM (Figure 3.4a) (Tarot, 2025). The second propeller had a diameter of $D = 0.64$. This propeller had winglets, to reduce the strength of the vortex generated by the wing, such that a more uniform flow hits the sandbed. The larger rotor experiment is also designed to investigate the threshold differences (fluid vs. impact threshold and hysteresis effects). Finally,This propeller can be seen in (Figure 3.4b) (Tmotor, 2025a).

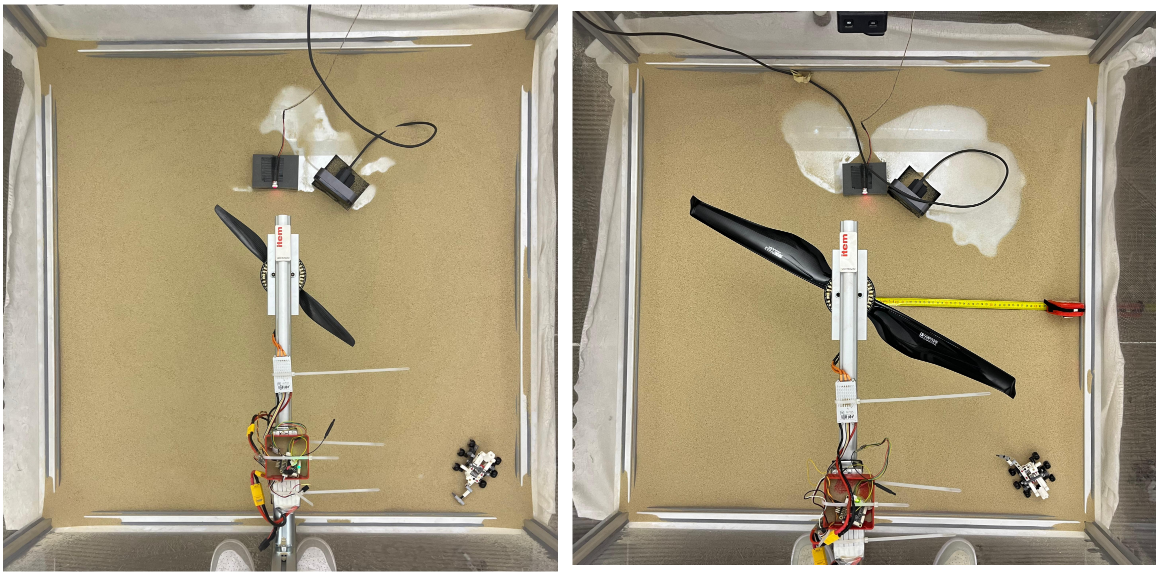

Figure 3.4: Rotor setup in the test box with (a) the small propeller ($D = 0.35$ m) and (b) the large propeller ($D = 0.64$ m). Shown are the adjustable mounting rod, motor mount, control box, sandbed, laser & camera setup, and a LEGO Technic 30682 piece in the lower right corner for scale.

Electronics Architecture

The electrical architecture consisted of a rechargeable 22.2 V, 4500 mAh LiPo battery, powering the ESC that controlled the BLDC motor; a second battery was kept as spare for sustained high-RPM operation at low density. Batteries were stored in a protective casing inside the chamber and replaced before each run to avoid voltage sag. A Universal Battery Elimination Circuit (UBEC) supplied regulated voltage to the Paparazzi flight controller and sensors. The motor was a BLDC 150 kV type, paired with a 40 A ESC. To prevent overheating, the ESC was positioned within the propeller slipstream to ensure convective cooling even under low-pressure operation (Tmotor, 2025b). A schematic overview of the electrical layout is provided in Figure 3.5.

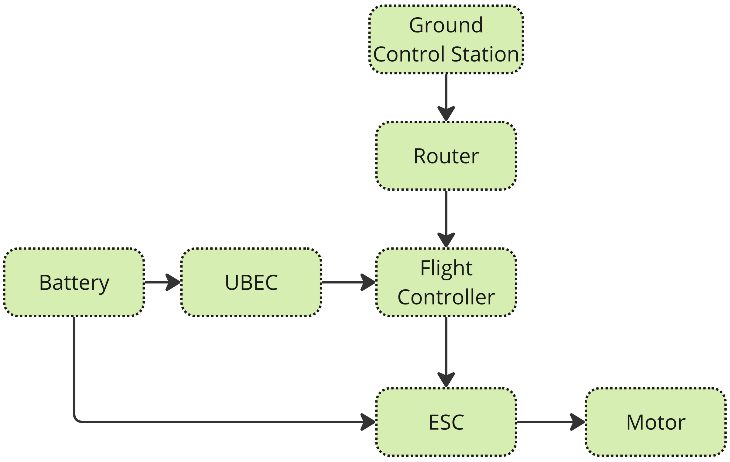

Figure 3.5: Schematic overview of the electrical architecture and data connections.

Control and Telemetry

One of the biggest challenges of the design of this experiment, was the limited wired connections between the inside en outside of the chamber. Also, due to the thick walls of the chamber, a wireless connection to control the rotor setup, was not an option. Eventually, there was a wired fibreglass feedthrough from a wifi-router inside the chamber that provided a reliable link to the laptop outside the chamber, from which the rotor could be operated. The rotor speed was controlled by the Paparazzi autopilot in manual-throttle mode, with outputs sent directly to the ESC a. The software logged all control inputs and timestamps, which were later synchronised with video and sensor data for analysis. This remote control system can be seen in (Figure 3.6).

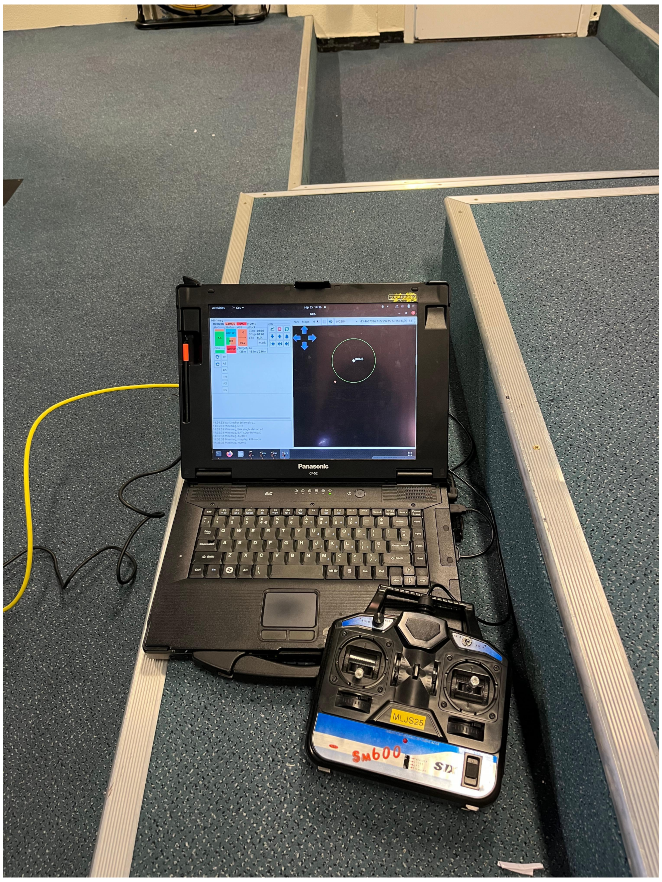

Figure 3.6: Remote control station for the rotor setup (outside the chamber) connected via fibre link to the in-chamber router.

3.1.4. Sediment Material

The granular material used to simulate Martian saltation-relevant sizes underwent a careful selection process. The aim was to choose an analogue that is safe to handle, behaves similarly to natural aeolian sand, and is available in sufficient quantities. The trade-off study and preparation procedures are outlined below. Candidate materials included natural quartz sand, volcanic ash/crushed volcanic glass, ground walnut shells, glass microspheres, and commercially available Mars regolith simulants.

Trade-Off Method

Options were evaluated against weighted criteria in a matrix. Scores ranged from 0 (poor) to 3 (best fit), with colour coding: *green* (3), *yellow* (2), *orange* (1), *red* (0). A weighted scoring was used to select the optimal material; improvements from red→orange or orange→yellow were prioritised, as yellow indicates requirements are met. Column widths in the table reflect criterion weight (% of 100). Method cf. van der Voort *et al.* (2022).

Trade-Off Criteria

- **Grain Shape (30):** Rounded grains roll and lift more easily than angular ones, lowering the threshold. This is especially relevant for Mars, where sands are typically rounded to well-rounded due to prolonged transport.
- **Cohesive Forces (30):** Electrostatic and van der Waals forces increase with finer sizes and dryness; these become relatively more important at low pressure.
- **Size Distribution (20):** Narrow distributions improve repeatability and comparability with theory.

- **Aeolian Suitability (10):** Behaviour should be comparable to natural wind-blown sand for relevance to desert and planetary conditions.
- **Particle Density (10):** Higher density increases the force required for entrainment.

Detailed Grain Comparison

Table 3.1 presents the assessment.

Table 3.1: Trade-off table for grain material.

Material	Grain Shape	Size Distribution	Particle Density	Cohesion / Electrostatics	Aeolian Representativeness
Quartz Sand (Andreotti *et al.*, 2021; Greeley, 2002; Zafiropoulos, 2025)	sub-rounded, natural Green	narrow 50–500 μm Green	2650 kg/m^3 Yellow	low when dry Yellow	dune-formed, natural Green
Volcanic Glass (de Vet *et al.*, 2014)	angular, irregular Orange	broad range Red	2800–3000 kg/m^3 Yellow	cohesive, fine Red	limited mobility due to cohesion Yellow
Walnut Shells (Greeley *et al.*, 1976, 1980)	fibrous, irregular Orange	broad, variable Red	$\sim$1200 kg/m^3 Red	electrostatic tendencies Orange	too light and oddly shaped Red
Glass Microspheres (Merrison *et al.*, 2007; B. R. White, 1979)	perfectly spherical Green	monodispersed Green	adjustable Yellow	non-cohesive Green	unrealistically smooth Orange
Mars Simulant (Technologies, 2025)	angular fragments Red	moderate sieve Orange	2700–3000 kg/m^3 Yellow	fine, cohesive Red	clumps due to cohesion Green

Based on this trade-off, both quartz sand and glass microspheres were suitable. The target was to find a realistic aeolian analogue while remaining controllable in the laboratory. Quartz sand was selected primarily due to its natural aeolian origin and availability. Since quartz sand from Soestduinen was freely available, it was chosen as the granular analogue for its availability, safety, and well-characterised aeolian behaviour.

Collection and Preparation

Approximately 15 kg of surface sand was collected, sealed, and oven-dried at 100 □ for 2 hours to remove moisture. After cooling, the sample was sieved up to 500 μm to remove debris, then stored in airtight containers. Before each run, a uniform 2 cm layer was placed in the box and levelled. Zafiropoulos (2025) performed size-distribution analysis on quartz sand from the Bedafse Bergen. As Bedafse Bergen and Soestduinen sands are geomorphologically similar, that distribution was used as a proxy for the Soestduinen sample. He concluded that for grains in the 50–500 μm range, the average diameter is $\sim$200 μm.

Figure 3.7: Landscape of Soestduinen.

Figure 3.8: Quartz sand collection in Soestduinen.

3.1.5. Measurement Systems

Two instrument systems were used to detect and characterise the onset of saltation and the near-surface flow.

Laser Sheet and Imaging

A laser diode formed a thin light sheet across the sand bed. A camera was positioned at a 45° angle relative to the laser plane for stereoscopic visibility. Chamber lights were kept off during runs to enhance the contrast of scattered light from airborne grains. The images were processed in ImageJ (Fiji) to detect the onset of particle motion via frame-by-frame intensity mapping, to approximate how much sand was moved. The laser diode and camera setup can be seen in Figure 3.9.

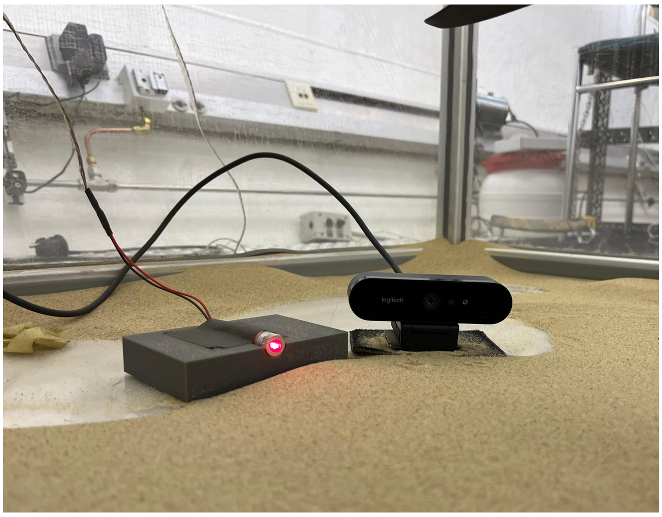

Figure 3.9: Laser-diode and camera arrangement used for threshold detection via light-sheet imaging and motion analysis.

Anemometry

Figure 3.10: Anemometer.

A fan-anemometer measured the vertical velocity field under the rotor. It was placed 5 mm above the ground, to measure the wind stream velocity hitting the sandbed.

3.2. Experiments

Three rotor configurations were tested, combining two rotor diameters and different heights above the bed. These configurations were selected to probe how rotor diameter and rotor height affect the near-surface shear stress and therefore the threshold for particle entrainment. All tests followed a consistent procedure to ensure reproducibility.

Test Configurations

Experiments were conducted for the following configurations:

1. **Small rotor:** $D = 0.35$ m, at $h = 0.5D$,
2. **Small rotor:** $D = 0.35$ m, at $h = 1.0D$,
3. **Large rotor:** $D = 0.64$ m, at $h = 0.5D$.

Each configuration was subjected to the same series of pressure levels and method. The chamber environment was systematically controlled to allow repeatable and directly comparable results.

Procedure

For each run, the hypobaric chamber was first evacuated to the desired target pressure while the rotor remained switched off. This ensured that the sand bed was not disturbed during pump-down. Once the target pressure was reached and stabilised, the rotor was powered on and the throttle was gradually increased until the first signs of saltation were observed on the live video recording of the laser & camera setup. This was visible, as the moving sand grains lifted through the laser sheet, causing a reflection of the grains into the camera. At that moment, the corresponding rotor speed (RPM), chamber pressure, and video timestamp were recorded.

After each test, the chamber was slowly re-pressurised back to Earth ambient (1013 mbar). This allowed the sand bed to be re-levelled and smoothed, as grain transport during saltation caused the sandbed to become uneven. The process was then repeated for the next pressure level.

The following pressure levels were used for all configurations: 1013 mbar (Earth ambient), 720 mbar, 480 mbar, 240 mbar, and 79 mbar. While these pressures are above Martian ambient, they represent a progressive reduction in density that is useful for examining scaling behaviour and for comparison with theoretical models that predict threshold dependence on air density.

Reverse-Pressure Tests

In addition to the standard downward pressure sweeps, reverse-pressure tests were conducted. The chamber was first pumped down to 79 mbar, after which the rotor was operated at maximum power. The pressure was then gradually increased until the first visible saltation occurred. This approach provided additional reference points for threshold validation and allowed comparison of entrainment behaviour during both decreasing and increasing pressure sequences.

Test Matrix

An overview of the configurations and pressure sweeps is shown in Table 3.2.

Table 3.2: Summary of rotor configurations and pressure sweep types.

Rotor Diameter	Rotor Height	Sweep Type	Pressure Range (mbar)
0.35 m	0.5D	Normal and reverse	1013 → 79
0.35 m	1.0D	Normal and reverse	1013 → 79
0.64 m	0.5D	Normal and reverse	1013 → 79

Consistency and Observations

To ensure data quality, the following procedures were applied consistently:

- The sand bed was re-prepared after each test to restore a smooth, level surface.
- The propeller, battery, motor, sensors, and electronics were checked for damage or debris.
- The throttle was increased slowly to precisely identify the saltation threshold without overshoot.

Representative snapshots before and after a test run are provided in Figure 3.11 and Figure 3.12.

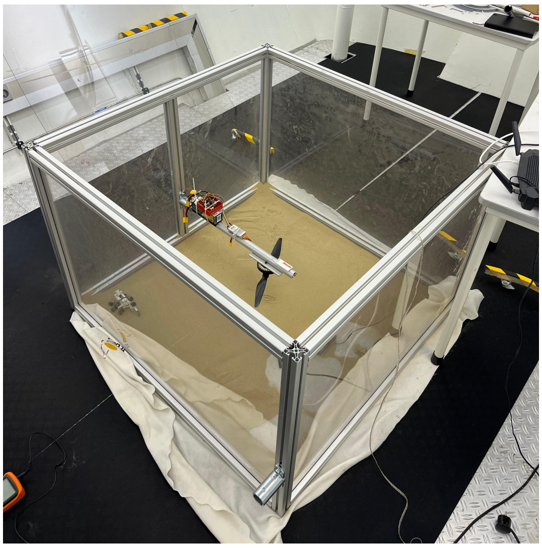

Figure 3.11: Complete assembly of the setup in the hypobaric chamber.

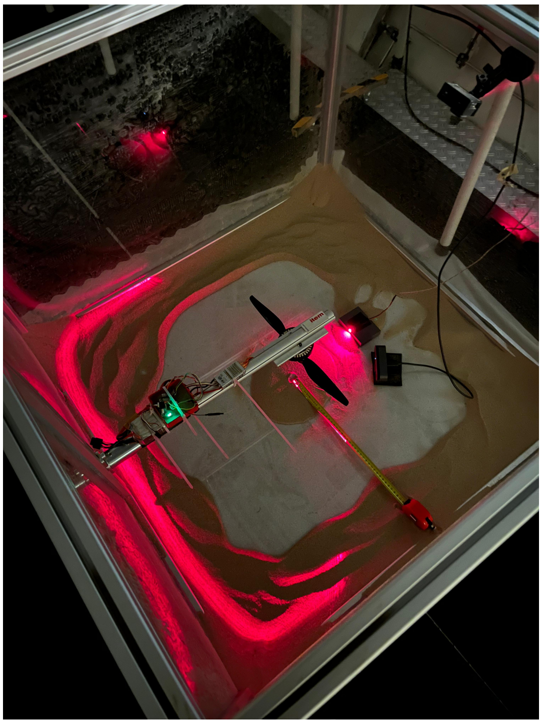

Figure 3.12: View of the assembly with the laser on and lights off after a test run.

3.3. Data Analysis

The primary experimental outputs were rotor speed (RPM), near-bed wind speed $u(z)$, and chamber pressure/temperature. These data were transformed for comparison with theory as follows:

1. Applied actuator disk theory to estimate thrust for each run:

$$T = \tfrac{1}{2}\,\rho\,A\,(v_e^2 - v_0^2), \tag{3.1}$$

   where $A = \pi R^2$ is the propeller (disk) area, v_e the exit velocity produced by the propeller, and v_0 the freestream velocity (NASA, 2025). It is assumed that the exit velocity is equal to the measured windspeed. Also, since there is no other wind stream present in the chamber, the freestream velocity is equal to 0. This step is necessary as one of the inputs of the Rabinovitch model is the thrust produced.

2. All other parameters, including the logged RPM, were used in the Rabinovitch model to estimate the friction velocity u_* generated by the rotor configuration.
3. Independently, the same measured wind speed was used with the logarithmic law-of-the-wall to calculate u_*:

$$u(z) = \frac{u_*}{\kappa}\,\ln\!\left(\frac{z}{z_0}\right), \tag{3.2}$$

   using $\kappa = 0.41$ and $z_0 = d_p/30$, where d_p is the representative particle diameter (Kok, 2010).

4. The computed u_* values were compared against theoretical entrainment thresholds from (Kok, 2010; Rabinovitch *et al.*, 2021; Shao & Lu, 2000).
5. Visualised the experimental thresholds by frame-by-frame analysis of the first visible grain motion in the laser sheet.
6. u_* was plotted versus ρ to evaluate scaling behaviour and identify deviations from theory.

All datasets were processed in Python using NumPy and Matplotlib. A flow diagram of all the parameters used in the model is provided below.

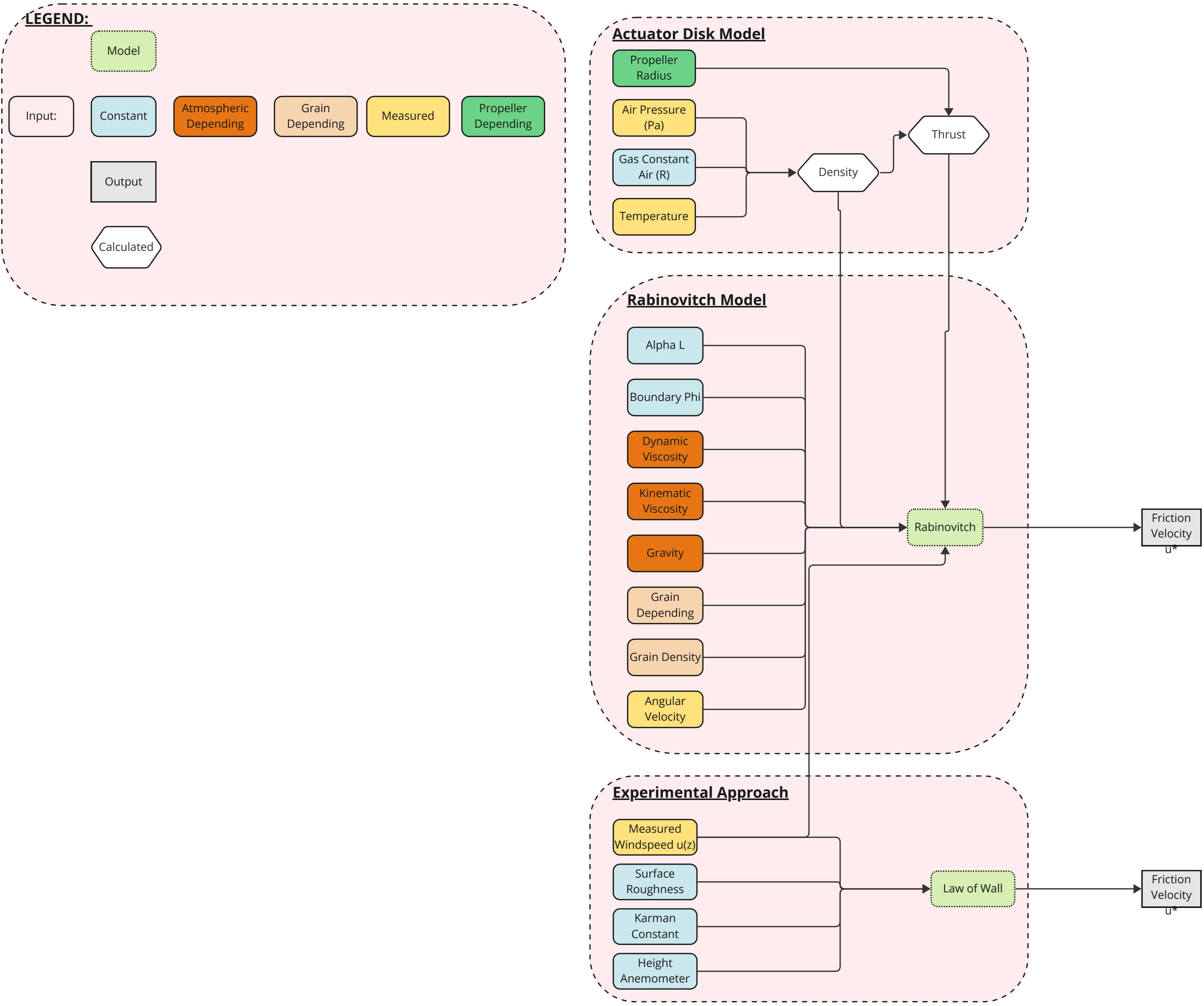
LEGEND:
Model
Input:
Constant
Atmospheric Depending
Grain Depending
Measured
Propeller Depending
Output
Calculated
Actuator Disk Model
Propeller Radius
Air Pressure (Pa)
Gas Constant Air (R)
Temperature
Density
Thrust
Rabinovitch Model
Alpha L
Boundary Phi
Dynamic Viscosity
Kinematic Viscosity
Gravity
Grain Depending
Grain Density
Angular Velocity
Rabinovitch
Friction Velocity u*
Experimental Approach
Measured Windspeed u(z)
Surface Roughness
Karman Constant
Height Anemometer
Law of Wall
Friction Velocity u*

4

Results

This chapter presents the experimental and theoretical findings on sand movement under varying atmospheric conditions. First, theoretical threshold wind speeds for sand movement are calculated using established models from Shao and Lu (2000) and Kok *et al.* (2012). Next, results from small-scale rotor experiments are detailed for two different rotor heights (h_1 and h_2 above the sand bed). This is followed by results from a larger rotor experiment designed to investigate threshold differences (fluid vs. impact threshold and hysteresis effects), as motivated in Chapter 3. All processed datasets, figures, and analysis scripts used in this chapter are provided in Appendix B, Appendix C, Appendix D, and Appendix E.

4.1. Threshold Predictions by Shao and Kok Models

The minimum friction velocity required to initiate sand saltation was first estimated using two theoretical models: the model by Shao & Lu (2000) for static (fluid) threshold and the model by Kok (2010) for both fluid and impact (dynamic) thresholds, as described in Chapter 2. Calculations were performed for three representative particle diameters corresponding to the minimum, median, and maximum grain sizes in the sand sample (50 μm, 200 μm, and 500 μm). Air density ρ was varied from approximately Earth-atmosphere density $\rho \approx 1.18$ kg/m^3 down to $\rho \approx 0.09$ kg/m^3 to examine how threshold wind speed changes in thinner air.

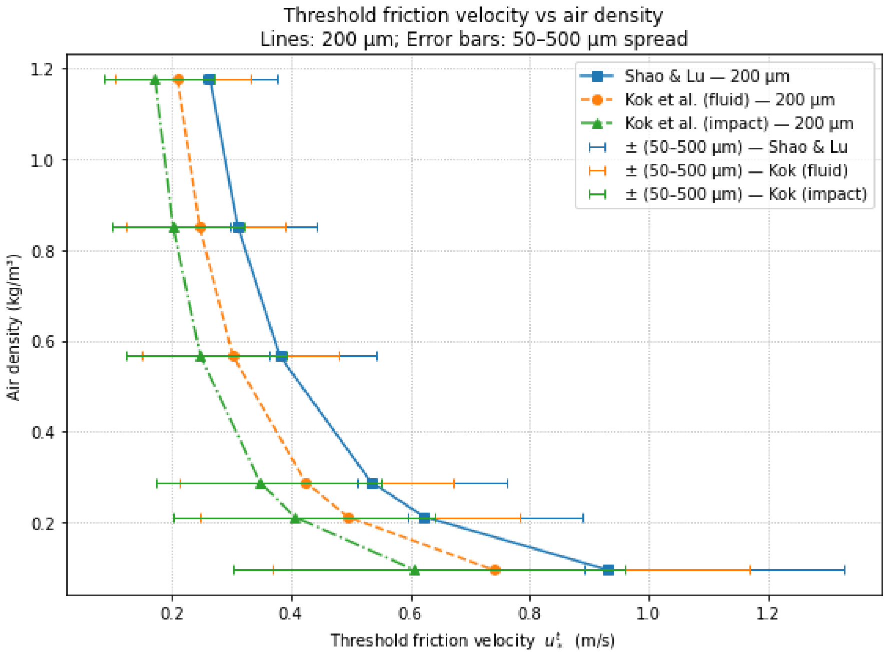

Figure 4.1: Threshold friction velocity vs. air density for 50 µm, 200 µm, and 500 µm grains, comparing Shao and Lu (2000) and Kok *et al.* (2012) models.

As expected, all models predict that the threshold friction velocity u_* required to initiate saltation rises sharply as air density decreases (see Figure 4.1). For example, for 200 µm grains at Earth-like density ($\rho \approx 1.18$ kg/m^3), the Shao & Lu model gives a threshold $u_* \approx 0.26$ m/s, while Kok's fluid threshold is slightly lower at ≈ 0.21 m/s. However, at a much lower density $\rho \approx 0.16$ kg/m^3, the predicted thresholds increase to $u_* \approx 0.73$ m/s (Shao & Lu) and 0.58 m/s (Kok fluid), reflecting the greater wind needed in thinner air. The impact threshold as calculated by Kok *et al.* (2012) is consistently lower than the fluid threshold. For 200 µm grains at $\rho \approx 0.16$ kg/m^3, it is about 0.47 m/s, as can be seen in Table B.1. The grains that are in motion cause an impact that ejects additional particles, reducing the wind required to sustain transport.

The model predictions also highlight the influence of grain size. At Earth density, the smallest grains (50 µm) are harder to mobilize than medium sand (200 µm) according to Shao & Lu's model due to interparticle cohesion. For 50 µm, $u_* \approx 0.28$ m/s vs. 0.26 m/s for 200 µm. In contrast, Kok's model predicts a lower threshold for 50 µm at Earth density (about 0.11 m/s fluid threshold). For large grains (500 µm), both models predict higher thresholds (around 0.33 m/s for Kok fluid, 0.38 m/s for Shao & Lu at Earth density) since heavier grains require stronger winds to lift. At lower densities ($\rho \approx 0.09$ kg/m^3), all thresholds become extremely high. For 500 µm grains, Shao & Lu's predicted $u_* \approx 1.33$ m/s, whereas Kok's fluid threshold is ≈ 1.17 m/s (with impact threshold ≈ 0.96 m/s). Even for fine grains (50 µm) at $\rho \approx 0.09$ kg/m^3, Shao & Lu predicts nearly 1.0 m/s threshold, while Kok's impact threshold is much lower (≈ 0.30 m/s).

In summary, decreasing the air density increases the wind speed required to initiate sand movement. There is also a clear hysteresis between initiation and continuation of saltation. Kok's impact threshold (for sustained motion) is about 15–30% lower than the fluid threshold for the same grain size and density. These theoretical expectations are compared with experimental findings in the following sections. Complete tables of calculated threshold values for all densities and grain sizes are provided in Appendix B.

4.2. Small Rotor Experiment at Height h_1

Threshold wind speeds were next investigated experimentally using the small rotor, as discussed in Chapter 3. At height $h_1 = R = 0.175$ m, the rotor was used to generate wind shear until sand motion was observed. The ambient pressure (and thus air density) was varied in a hypobaric chamber, and for each pressure the rotor speed (in RPM) was slowly increased until the onset of particle movement (the fluid threshold) was detected. This procedure was repeated for the three representative grain sizes (50 µm, 200 µm, 500 µm). The corresponding rotor thrust and the pressure drop across the rotor were approximated using the actuator disk model (explained in Chapter 3), and a near-surface anemometer measured the wind speed $u(z)$ at $z = 5$ mm above the bed.

Using the measured $u(z)$ and assuming a roughness length $z_0 = d_p/30$ (where d_p is particle diameter, following Kok (2010)), the friction velocity at threshold was estimated via the Law of the Wall. For comparison, an independent estimate of the shear velocity was obtained from the rotor performance using the method of Rabinovitch *et al.* (2021). The Law-of-Wall estimate uses the local measured $u(z)$ to infer the mean shear at the bed, while the Rabinovitch estimate uses rotor parameters to approximate the peak shear generated by the downwash velocity.

Table 4.1 summarises the threshold conditions at various air densities for each grain size, including both the Law-of-Wall and Rabinovitch estimates of u_*. Figure 4.2 and Figure 4.3 show air density versus generated friction velocity for the small rotor at h_1 for each method.

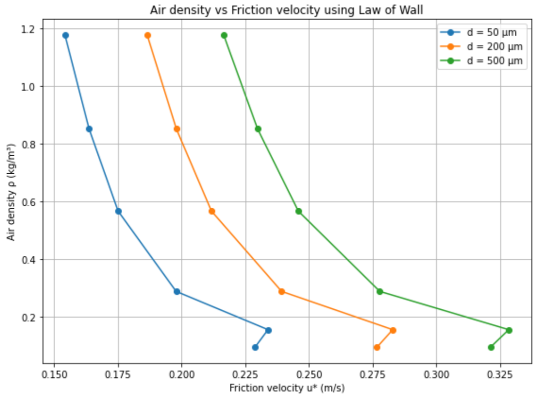

Figure 4.2: Calculated friction velocity u_* vs. air density for the small rotor at h_1, for 50, 200, and 500 µm grains using the Law of the Wall method.

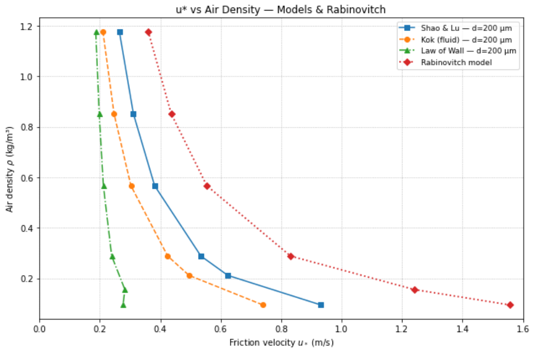

Figure 4.3: Calculated friction velocity u_* vs. air density for the small rotor at h_1, for 200 µm grains, Rabinovitch method.

At the highest air density tested (approximately $\rho = 1.18$ kg/m^3, near ambient Earth conditions), the small rotor initiated motion of all three grain sizes at relatively low rotor speeds (around 1600 RPM for 50 µm sand, see Table 4.1). The corresponding threshold friction velocities (using Law of the Wall) were $u_*^{\text{LoW}} \approx 0.15$–$0.22$ m/s, in reasonable agreement with the theoretical predictions for Earth conditions from Section 4.1. The smallest grains (50 µm) had the lowest threshold $u_* \approx 0.154$ m/s, whereas the largest grains (500 µm) required about 0.217 m/s to start moving. The medium-sized grains (200 µm) fell in between, needing $u_* \approx 0.187$ m/s at Earth density.

As the air density was reduced, the rotor had to spin faster to achieve threshold. For example, at $\rho \approx 0.57$ kg/m^3 (about half of Earth's density), the threshold rotor speed for 50 µm grains increased to about 1926 RPM, corresponding to $u_*^{\text{LoW}} \approx 0.175$ m/s. At $\rho \approx 0.16$ kg/m^3, the threshold occurred at nearly full throttle (2889 RPM for 50 µm), giving $u_*^{\text{LoW}} \approx 0.234$ m/s. The largest grains similarly required increasingly higher RPM and u_* as density dropped (500 µm grains needed $u_*^{\text{LoW}} \approx 0.328$ m/s at $\rho \approx 0.16$ kg/m^3). Quantitatively, the measured threshold friction velocities as a function of density align reasonably well with Kok's fluid threshold model, whereas Shao & Lu's model tends to overpredict the needed u_* for the finer grains.

For each condition, the Rabinovitch method yielded a second estimate of the threshold shear velocity (u_*^{Rab} in Table 4.1). In Figure 4.3 it can be seen that u_*^{Rab} is consistently higher than the Law-of-Wall estimate u_*^{LoW} for the same event, and the difference grows with decreasing density. Possible reasons for the divergence between the two estimates are examined in Chapter 5.

At the lowest density tested ($\rho \approx 0.095$ kg/m^3), the small rotor did not initiate motion for any of the grain sizes. Even at maximum RPM (2900), no sustained saltation was observed. The last row for each grain size in Table 4.1 lists the maximum attained flow conditions without a corresponding threshold RPM. Extrapolating from the models and the Rabinovitch estimate ($u_*^{\text{Rab}} \approx 1.56$ m/s at $\rho = 0.095$ kg/m^3), the fluid threshold at this density is beyond what the small rotor could produce.

Table 4.1: Threshold conditions for saltation in the small rotor experiment at height h_1. Data are shown for multiple ambient air densities (in kg/m^3) and three grain sizes. For each condition, the near-bed wind speed $u(z{=}5$ mm$)$, the friction velocity from the Law of the Wall (u_*^{LoW}), the rotor pressure drop Δp, rotor thrust T, and the rotor speed at threshold (RPM) are given. Also shown is the friction velocity u_*^{Rab} estimated via the Rabinovitch method.

Particle diameter	ρ (kg/m^3)	$u(z)$ @ 5 mm (m/s)	u_*^{LoW} (m/s)	Δp (Pa)	T (N)	RPM (at threshold)	u_*^{Rab} (m/s)
50 µm	1.18	3.01	0.154	5337	0.513	1596	0.36
	0.85	3.20	0.164	4348	0.418	1746	0.44
	0.57	3.42	0.175	3314	0.319	1926	0.55
	0.29	3.86	0.198	2150	0.207	2278	0.83
	0.16	4.57	0.234	1627	0.157	2889	1.24
(no motion)	0.095	4.45	–	939	0.090	(max) 2900	1.56
200 µm	1.18	3.01	0.187	5337	0.513	1596	0.36
	0.85	3.20	0.198	4348	0.418	1746	0.44
	0.57	3.42	0.212	3314	0.319	1926	0.55
	0.29	3.86	0.239	2150	0.207	2278	0.83
	0.16	4.57	0.283	1627	0.157	2889	1.24
(no motion)	0.095	4.45	–	939	0.090	(max) 2900	1.56
500 µm	1.18	3.01	0.217	5337	0.513	1596	0.36
	0.85	3.20	0.230	4348	0.418	1746	0.44
	0.57	3.42	0.246	3314	0.319	1926	0.55
	0.29	3.86	0.278	2150	0.207	2278	0.83
	0.16	4.57	0.328	1627	0.157	2889	1.24
(no motion)	0.095	4.45	–	939	0.090	(max) 2900	1.56

4.3. Small Rotor Experiment at Height h_2

The small rotor experiments were repeated with the rotor raised to a higher altitude h_2 above the sand bed (approximately twice the height of h_1). The procedure remained the same: at each ambient pressure, increase rotor RPM until saltation begins, record the threshold conditions, then estimate u_* via Law-of-Wall and Rabinovitch methods. The results for h_2 were qualitatively similar to the h_1 case, and are summarised in Table 4.2. Similar friction velocity over density plots are shown in Figure 4.4 corresponding to the law of wall method, and Figure 4.5 to Rabinovitch's method.

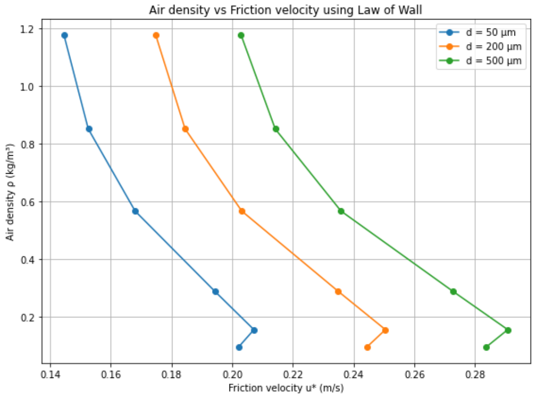

Figure 4.4: Calculated friction velocity (or u_*) vs. air density for small rotor at h_2, for 50, 200, 500 µm grains using the Law of Wall method.

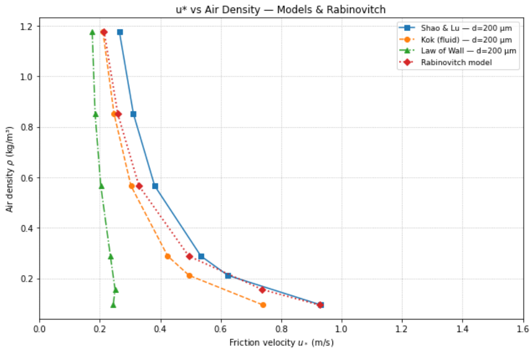

Figure 4.5: Calculated friction velocity (or u_*) vs. air density for small rotor at h_2, for 200 µm grains.

The data in Table 4.2 show that the threshold friction velocities (u_*^{LoW}) required for each grain size at a given density were essentially the same as those at h_1. For example, at $\rho \approx 1.18$ kg/m^3, 50 µm grains again required $u_*^{LoW} \approx 0.154$ m/s to initiate motion, and 500 µm grains about 0.217 m/s. This consistency indicates that the threshold condition is predominantly a function of the grain and fluid properties, not the rotor height per se. In other words, the minimum shear stress to lift the grains is unchanged by moving the rotor further from the surface.

However, the rotor speed (RPM) and thrust needed to reach that shear stress did increase at the greater height. At Earth-like density, the fluid threshold for 50 µm occurred around 1682 RPM at h_2, compared to only 1596 RPM at h_1. Similarly, at $\rho \approx 0.29$ kg/m^3, threshold for 50 µm was reached at 2595 RPM at h_2 versus 2278 RPM at h_1. The higher RPM reflects the fact that with more distance, the rotor's downwash spreads out and exerts less intense stress on the surface, so more power is required to achieve the same u_*. This is evident in the measured near-bed wind speeds as well: at h_2, the wind speed at 5 mm was slightly lower for the same friction velocity compared to h_1 (*e.g.*, $u(z) = 2.82$ m/s for $u_*^{LoW} = 0.154$ m/s at h_2, whereas it was 3.01 m/s at h_1 for the same u_*). The broader, less focused flow from the higher rotor likely led to a more uniform but weaker shear distribution.

The Rabinovitch shear velocity estimates at h_2 were also closer to the Law-of-Wall values than they were at h_1. For instance, at $\rho \approx 1.18$ kg/m^3 and 50 µm, $u_*^{Rab} \approx 0.19$ m/s vs 0.154 m/s (only 25% higher). Compare this to h_1 where u_*^{Rab} was over 2 times u_*^{LoW}. This suggests that at the higher rotor height, the flow at the surface was more akin to a conventional wind profile (the rotor's influence is less concentrated), making the Law-of-Wall assumption more valid and narrowing the gap between the two methods. At lower densities, u_*^{Rab} at h_2 was still larger than u_*^{LoW} (*e.g.*, for 50 µm at $\rho \approx 0.16$, $u_*^{Rab} = 0.55$ m/s vs 0.234 m/s), but the factor difference (2.3) is less extreme than the factor 5 observed at h_1. Essentially, raising the rotor reduced the spatial variability of the shear stress, making the point measurement more representative of the overall stress field.

As with the h_1 tests, no grain movement could be initiated at the lowest density $\rho \approx 0.095$ kg/m^3, even at maximum rotor speed. The threshold friction velocity at that density is simply too high for the small rotor. Overall, the h_2 experiments confirm the trends seen at h_1. The difference is that a rotor operating farther from the bed must work harder (higher RPM/thrust) to achieve that u_*.

Table 4.2: Threshold conditions for the small rotor at the higher altitude h_2. Columns are analogous to Table 4.1. The threshold friction velocities required are similar to those at h_1, but higher rotor RPMs were needed to achieve them due to the increased rotor height.

Particle diameter	ρ (kg/m^3)	$u(z)$ @5mm (m/s)	u_* LoW (m/s)	Δp (Pa)	T (N)	RPM (at threshold)	u_* Rab (m/s)
50 μm	1.18	2.82	0.154	4685	0.451	1682	0.19
	0.85	2.98	0.164	3774	0.363	1832	0.23
	0.57	3.48	0.175	3433	0.330	2300	0.31
	0.29	3.79	0.198	2072	0.199	2595	0.45
	0.16	4.04	0.234	1734	0.167	2889	0.55
(no motion)	0.095	–	–	–	–	(max) 2900	–
200 μm	1.18	2.82	0.187	4685	0.451	1682	0.19
	0.85	2.98	0.198	3774	0.363	1832	0.23
	0.57	3.48	0.212	3433	0.330	2300	0.31
	0.29	3.79	0.239	2072	0.199	2595	0.45
	0.16	4.04	0.283	1734	0.167	2889	0.55
(no motion)	0.095	–	–	–	–	(max) 2900	–
500 μm	1.18	2.82	0.217	4685	0.451	1682	0.19
	0.85	2.98	0.230	3774	0.363	1832	0.23
	0.57	3.48	0.246	3433	0.330	2300	0.31
	0.29	3.79	0.278	2072	0.199	2595	0.45
	0.16	4.04	0.328	1734	0.167	2889	0.55
(no motion)	0.095	–	–	–	–	(max) 2900	–

4.4. Large Rotor Experiments

To further investigate threshold behaviour, especially the distinction between fluid and impact thresholds (hysteresis), experiments were conducted with a larger rotor in the hypobaric chamber. The large rotor is capable of generating stronger winds and was tested at low ambient pressures. Two complementary tests were performed.

Test 1: Fluid vs. Impact Threshold at Constant Pressure.

The ambient pressure was set to 240 mbar (approximately $\rho \approx 0.29$ kg/m^3). Rotor throttle was gradually increased until intense sand movement was observed (the fluid threshold for that pressure). After sustained saltation was achieved, rotor throttle was slowly reduced until transport ceased (impact threshold). Rotor thrust, RPM, and wind conditions were recorded. The difference between the onset and cessation points identifies the gap between the fluid and impact thresholds at 240 mbar.

The results of Test 1 showed a clear difference between the fluid and impact thresholds at 240 mbar. Sand movement initiated at a rotor setting of approximately 81% throttle (about 2070 RPM), but once saltation was in full effect, rotor speed could be reduced to about 64% throttle (around 1650 RPM) before transport stopped. In terms of shear stress, the impact threshold was roughly 10-20% lower than the fluid threshold. The results of test 1 can be found in Table 4.3

Table 4.3: Raw threshold measurements for Test 1 (constant p).

Test	p [mbar]	Throttle [%]	RPM	Label
1 (const p)	240	81	2070	fluid
1 (const p)	240	64	1636	impact

Test 2: Threshold Hysteresis with Changing Pressure.

This test was inspired by the findings of Andreotti *et al.* (2021), who reported that once saltation is initiated at a given shear stress, it can continue even if conditions change such that the static threshold would not have been exceeded. The chamber was pumped to 110 mbar ($\rho \approx 0.13$ kg/m^3) and the fluid threshold rotor speed was found at that pressure. After saltation began at 110 mbar, rotor throttle was held constant and ambient pressure was increased to 240 mbar, which raised air density and led to vigorous saltation. Next, rotor throttle was reduced at 240 mbar until motion stopped. The focus is whether this final “stop” throttle was lower than the “start” throttle required.

In Test 2, saltation initiated at 240 mbar could be sustained at a much lower rotor speed once the pressure was decreased to 110 mbar. At 240 mbar the fluid threshold occurred at around 2070 RPM. After lowering the pressure to 110 mbar with the same throttle setting, the sand kept saltating, even though the same throttle was lower than the value needed to start from rest at 110 mbar. This demonstrates hysteresis.

Due to a battery issue, the second run of Test 2 could not be completed. However, the single run performed was sufficient to observe the key hysteresis behaviour.

4.5. Image Analysis of Sand Movement

The laser sheet served two roles. During threshold detection it was used in real time to identify the first visible grain crossings at the measurement plane. For visualisation, difference images were created by subtracting a “before” frame from a “during” frame to highlight the spatial extent of motion at or near threshold. The visualisation was not used to determine the threshold itself.

As described in Chapter 3, a camera and laser illumination were used to visualise where and how much sand movement occurred at threshold. Videos and images were captured of the sand bed both before any movement (static condition) and during active saltation for the same field of view. Using ImageJ, the “before” image was subtracted from the “during” image to produce a difference image highlighting regions of change. This difference image was further processed to clearly show the areas where sand grains had moved.

Figure 4.6: Image before saltation at 720 mbar with small rotor h_1.

Figure 4.7: Image during saltation at 720 mbar with small rotor h_1.

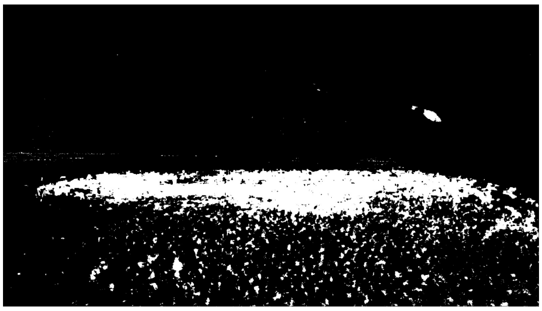

Figure 4.8: Processed difference image, showing regions of sand motion (bright) at 720 mbar with small rotor h_1.

Figure 4.8 shows the result of this image subtraction for an example case: the small rotor at h_1 operating at 720 mbar (approximately $\rho = 0.85$ kg/m^3), where sand motion was just initiated. In the processed image, bright spots indicate locations where the sand surface changed between the static and saltation conditions (i.e., grains were displaced or ejected). A roughly circular patch directly beneath the rotor where the most intense activity occurred, can be seen in Figure 4.9. This corresponds to the area of highest shear stress from the rotor downwash. Some grain motion is also visible slightly beyond the immediate rotor radius, likely due to saltating grains hopping and landing outside the main region or weak turbulent eddies carrying grains outward. The edges of the bright region are relatively sharp, suggesting a threshold-like condition: inside the region, the wind stress exceeded the threshold and grains moved; outside, the stress was below threshold and the bed remained undisturbed.

The image analysis provides a qualitative confirmation of the threshold measurements. At pressures like 720 mbar, the area of motion is confined and only a small fraction of grains are mobilized, consistent with being right at the threshold. At higher rotor speeds, it can be observed in other images that the bright region expands and more grains are transported. Next to that, the rotor-induced wind does not lift all grains uniformly, but creates localized spots of activity where the combination of turbulence and grain interactions triggers motion.

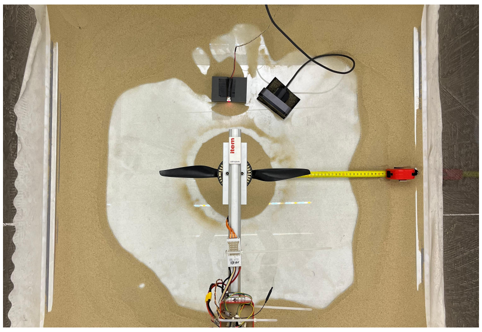

Figure 4.9: Circular patch forming.

5

Discussion

The experimental results show a clear dependence of the sand movement threshold on ambient pressure. As expected, lowering the air pressure (and thus density) increases the rotor speed (RPM) required to initiate grain motion. In terms of equivalent surface shear, the threshold friction velocity u_* tends to rise as pressure is reduced, since thinner air exerts less force on the grains for a given flow speed. This aligns with wind tunnel studies of aeolian transport under Martian conditions, which found that wind friction thresholds increase at lower atmospheric density (Merrison *et al.*, 2008). The measurements can be compared to those studies by relating the rotor-induced flow to an effective u_* at the surface. The friction velocity corresponding to each rotor RPM was estimated using a method analogous to that of Merrison and colleagues, who derived u_* from known flow characteristics in low-pressure wind experiments (Etyemezian *et al.*, 2007; Merrison *et al.*, 2008). This conversion allows to discuss the rotor results in the context of traditional threshold friction velocity data. Even though the required RPM increased at lower p, the absolute near-surface wind speeds generated by the rotor did not rise proportionally, due to the physics of rotor thrust in thin air. In practice, it was observed that at the lowest pressure tested the rotor nearly reached its maximum capable RPM before sand motion was observed. This underscores the challenge of lifting sand in a thin atmosphere: even operating at full power, the flow induced may barely reach the threshold needed to mobilise grains (Kok *et al.*, 2012; Shao & Lu, 2000).

5.1. Viscosity

One important consideration is the role of the fluid's (air) viscosity. In the theoretical approach of Rabinovitch *et al.* (2021), the kinematic viscosity of the gas was treated as a constant value. In reality, this is not a valid assumption for a wide range of pressures. The kinematic viscosity ν of a gas depends on both the dynamic viscosity (which is primarily a function of temperature) and the density ($\nu = \mu/\rho$) (F. White, 2016). As the pressure (and thus ρ) decreases, ν increases correspondingly for a given temperature. In an ideal gas, ν is roughly proportional to $T^{3/2}/p$, so at low pressures the gas becomes more viscous in terms of momentum diffusion. The experiments maintained roughly constant temperature (289 - 298 K), so dynamic viscosity μ was nearly constant while ρ dropped with pressure, leading to a higher ν in the low-p runs. This has implications for the threshold condition: higher kinematic viscosity can cause the initiation of motion for very small grains (those in the viscous regime), potentially raising the fluid threshold (Iversen & White, 1982). In Figure 5.1, it can be seen that the model of Rabinovitch, moves closer to the other models, if the viscosity is not considered a constant.

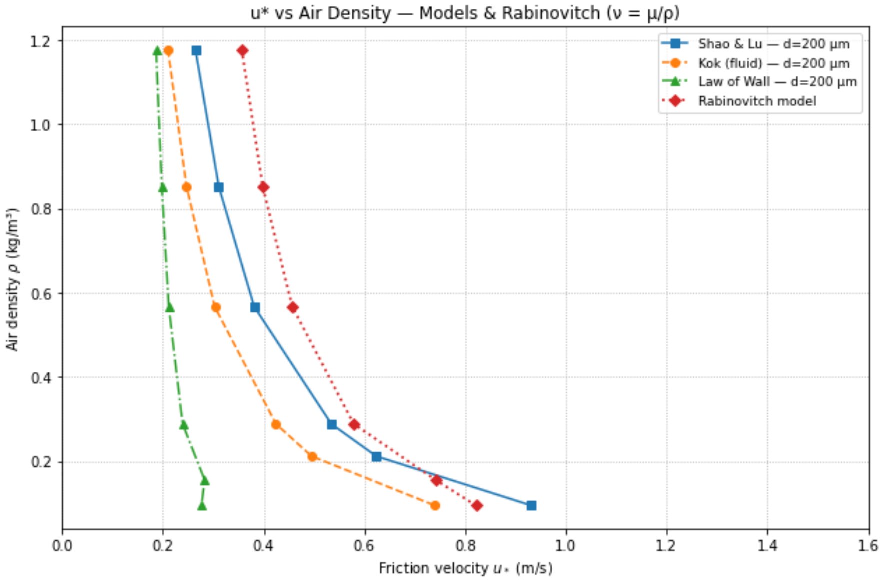

Figure 5.1: Calculated friction velocity (or u_*) vs. air density for small rotor at h_1, for 200 μm grains, using the kinematic viscosity as a pressure dependent parameter.

With the experiment, the sand grain diameter was approximately d_p = 200 μm. Grains of the size of $\approx$ 250 μm place the threshold in the inertia-gravity dominated regime, whereas smaller grains are more in the viscous regime (Iversen & White, 1982), so the direct effect of ν on threshold might have to be considered. However, it is worth acknowledging that any modelling that assumed a constant ν, such as Rabinovitch *et al.* (2021), would become increasingly inaccurate as density varies. A more precise analysis would implement the pressure-dependence of viscosity.

The model-data comparison conducted here shows that implementing the pressure dependence of kinematic viscosity is necessary to reproduce the observed thresholds in the low-pressure runs. Using $\nu(p)$ reduces the discrepancy between the analytical prediction and the measurements across the full density range tested, whereas a constant-ν assumption systematically overestimates u_* (see Figure 5.1). A more precise analysis should therefore include the pressure dependence of viscosity.

Across all checks performed for this chapter, incorporating $\nu(p)$ was the main modelling change that consistently reduced the model–measurement gap at every pressure level and rotor height. Inclusion of pressure-dependent kinematic viscosity is thus the primary finding to this study: without it, analytical predictions of u_* in thin air remain biased.

5.2. Grain Properties

Grain properties such as size and density also strongly affect the threshold. The measurements were conducted with a fixed sand sample (of particular grain size distribution and material density), but a sensitivity analysis can be instructive. Theory and prior experiments indicate that heavier or larger grains require a higher shear stress to lift (Bagnold, 1994; Iversen & White, 1982; Shao & Lu, 2000). In classic models of sediment transport, the threshold friction velocity u_{*t} scales with the square root of particle diameter for sufficiently large grains, making it more difficult for larger grains to entrain. This is because the gravitational force (scaling with grain volume) grows faster than the increase in aerodynamic drag force for bigger grains. The results would therefore likely shift if different sand were used: for instance, using very fine sand (or dust) would reduce the threshold u_*, whereas using coarser sand or gravel would increase it. Grain density plays a similar role: a denser mineral (higher ρ_p) is heavier for the same size and will have a higher threshold. The force balance at threshold is often expressed as a ratio of fluid lift/drag to grain weight, so a higher ρ_p or d shifts the balance towards needing stronger winds to initiate motion (Bagnold, 1994). It is known that Mars regolith typically has particles of basaltic density (3000 kg/m^3) similar to terrestrial sand, but the potential presence of very fine dust (tens of microns), could introduce much lower thresholds for dust compared to sand (Kok *et al.*, 2012). In summary, while the experiments focused on a single sand type, the threshold findings are not universal for all particle types. Future work could repeat the tests with varied grain sizes or densities to quantify these effects.

5.3. Gravity

Another environmental factor to consider is gravity. The experiments were conducted under Earth gravity ($g = 9.81$ m/s^2), whereas Martian gravity is only about 3.7 m/s^2. Reduced gravity lowers the weight of grains, which in principle should reduce the wind speed needed to lift them. The classical threshold models predict that u_{*t} is proportional to $\sqrt{\frac{(\rho_p-\rho_f)gd}{\rho_f}}$ for non-cohesive grains in high Reynolds number flow (Iversen & White, 1982). A lower g directly reduces the numerator of that expression, so one would expect a lower threshold on Mars if all other factors were equal. The effect of changing gravity towards Martian level is shown in Figure 5.2. This effect partly offsets the impact of Mars's thin atmosphere. Martian winds are even with the low air density able to move sand, such that dunes and ripples do migrate on Mars. The lower Martian gravity is a contributing factor that eases sediment motion. However, even accounting for gravity, early estimates suggested extremely high wind speeds would be required to mobilise sand on Mars. The results at low pressure reflect a similar challenge: despite Earth gravity helping to hold grains down more strongly than Mars would, it was still difficult to initiate motion as density dropped. If the same rotor experiment would be conducted under reduced gravity (*e.g.*, in a drop tower or aircraft), it is expected that the threshold RPM (or u_*) will decrease somewhat. In the absence of such data, one could rely on extrapolation and Martian analogue studies: for example, Merrison *et al.* (2008) measured threshold friction speeds around 2–3 m/s for sand at Martian atmospheric pressure (6–10 mbar CO$_2$) under Earth gravity, and argued that under Mars gravity the threshold would be even lower. *In-situ* observations by rovers have since confirmed that sand mobilization occurs on Mars under wind speeds lower than originally predicted by Earth-based models (Sullivan *et al.*, 2008). Thus, while the experiments quantify the pressure effect under terrestrial gravity, actual Martian operations benefit slightly from a gravity drop, but not enough to completely overcome the thin atmosphere's limitations.

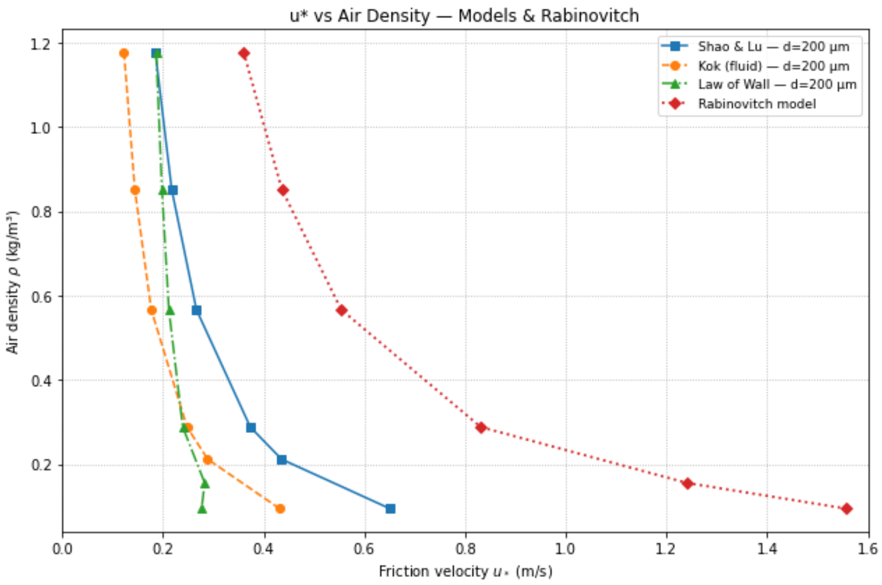

Figure 5.2: Calculated friction velocity (or u_*) vs. air density for small rotor at h_1, for 200 μm grains, using Martian gravity. The deviation from the Rabinovitch model has increased, since this model is indepedent of gravity.

5.4. Atmosphere

It is also important to consider the composition of the atmosphere in the experiments versus Mars. The experiments were done in air (primarily N$_2$/O$_2$). Mars' atmosphere is about 95% CO$_2$ with a mean molecular weight of 43.3 g/mol (compared to air's 28.8 g/mol) (Williams, 2025). At the same pressure and temperature, CO$_2$ has a higher density than air by roughly a factor of order unity (about 1.5 at room temperature). That statement is correct as a gas-property comparison, but laboratory practice does not hold both pressure and gas fixed when targeting Mars analogues.

For threshold experiments the primary similitude target is the flow, not the gas name. Matching air density ρ and the relevant dimensionless groups (notably particle Reynolds number and Shields parameter) can be achieved by adjusting pressure and temperature in either gas. A Mars-density CO_2 atmosphere at low pressure can be recreated with Earth air at a higher pressure under room temperature conditions, producing the same ρ and comparable kinematic viscosity ν for the grains tested. Wind-tunnel studies report that when these parameters are matched, thresholds and ripple properties measured in air overlap those in CO_2 within experimental uncertainty (Andreotti *et al.*, 2021; Merrison *et al.*, 2008, 2007).

The practical implication is that switching to CO_2 is not required to obtain Mars-relevant thresholds if ρ and the governing non-dimensional groups are matched. Using CO_2 can still be valuable when investigating composition-sensitive processes such as thermal or electrostatic effects, but threshold initiation itself is well captured by appropriately scaled air experiments (Andreotti *et al.*, 2021; Merrison *et al.*, 2008). In future work, the choice between CO_2 and air should therefore be guided by which quantities are being held fixed in the similitude design: if ρ and ν are matched, air suffices, but if gas-specific physics are of interest, CO_2 becomes beneficial.

5.5. Moisture

An experimental complication encountered was the creation of moisture. The sand used was initially dry; however, when the chamber rapidly decreased the pressure for low-p tests, fogging (mist) was observerd inside the chamber. The mist suggests that water vapor in the air was condensing due to the rapid expansion and cooling of the air. That condensation could settle on the sand grains, eventually moistening the soil. Even a small amount of moisture can significantly increase the cohesion between grains by forming liquid bridges (F. White, 2016). This leads to a higher threshold friction velocity, as the wind must overcome not just gravity but also capillary forces binding the grains (Shao & Klose, 2016). In the lowest-pressure runs, the presence of moisture might have raised the threshold. An attempt was made to mitigate this by pumping down more slowly, but some moisture effects may still have been present. This could partly explain any cases where the measured threshold at very low pressure was higher than expected. In future testing, baking the sample and using a dry gas purge could help eliminate this factor. The moisture could have introduced an upwards bias in threshold at low p, meaning the true dry threshold in those cases might be slightly lower than recorded. For future testing, it can be useful to weight the sand before and after the test, to see if any moist affected the mass of the sandbed.

5.6. Comparison to Models

Traditional models (*e.g.*, Shao and Lu (2000)) predict that as particle size increases, it becomes exceedingly difficult for the wind to lift grains. In such models, u_{*t} increases for large d roughly as $\propto \sqrt{d}$ (beyond the size of minimum threshold) (Bagnold, 1994; Shao & Lu, 2000). Kok (2010), focusing on the continuous saltation regime, similarly noted that very large grains would require very high fluid speeds to initiate movement. Both Shao's and Kok's formulations would suggest that, gravel-sized particles or heavier sand would be almost immobile under Martian wind conditions. However, more recent work by Andreotti *et al.* (2021) showed a new regime at extremely low air densities (or equivalently very high grain-to-fluid density ratios). In their experiments, which pushed to pressures as low as a few mbar in a wind tunnel, the threshold wind speed for sand did not continue to increase as steeply as older models extrapolated. In fact, they found a *lower-than-expected* threshold at Martian pressures and below. This suggests that collective effects or altered turbulence/grain interactions at low pressure enable motion at a relatively lower u_*. In other words, once the density ratio is beyond $\approx 4 \times 10^5$, the simple scaling breaks down and grains can be moved more easily than one would think from Earth data (Andreotti *et al.*, 2021). This finding is essentially the opposite of the earlier expectation that "heavier grains are always harder to move. It might be that interactions like aerodynamic instabilities or grain inertia effects reduce the needed lift. The pressure range of this experiment, might not have been low enough to fully enter the new regime identified by Andreotti *et al.* (2021). There was no sudden drop in friction velocity, causing the data to align more with the classical expectation. Figure 5.3 & Figure 5.4 contain a visual comparison of all the models for the small rotor setup at h_1 & h_2, respectively.

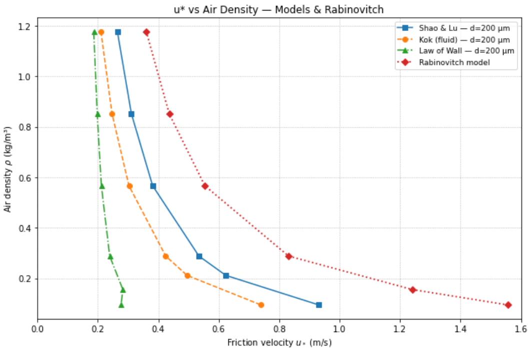

Figure 5.3: Calculated friction velocity (or u_*) vs. air density for small rotor at h_1, for 200 µm grains

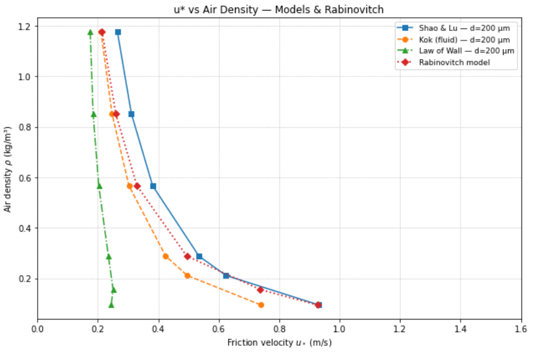

Figure 5.4: Calculated friction velocity (or u_*) vs. air density for small rotor at h_2, for 200 µm grains, using Martian gravity

5.7. Rotorcraft performance

The performance of the rotor itself under varying atmospheric density is another point of discussion. Flying in thinner air is challenging not just for grain lifting, but for the aircraft as well. As the pressure drops, the rotor experiences less aerodynamic drag, which allows it to spin faster. This is why the Ingenuity helicopter on Mars uses an extremely high rotor rotation rate (around 2400 RPM, roughly five times that of an equivalent terrestrial helicopter) (Koning & Dominguez, 2024). The low air density necessitates much greater blade speeds and larger rotor blades to generate sufficient lift (Koning & Dominguez, 2024). In this experiment, it was observed that achieving thrust at low pressure demanded very high RPMs. However, even though the blades can spin faster with less resistance, the mass flow of air being accelerated is much lower. In hover, the thrust T of a rotor is related to the mass of air displaced per time and the induced velocity v_i imparted to that air ($T = \dot{m} v_i$). For a rotor of disk area A, $\dot{m} = \rho A v_i$. Combining these, $T = \rho A v_i^2$. Solving, the induced velocity in hover is $v_i = \sqrt{T/(\rho A)}$ (Leishman, 2006). Thus, to produce the same lift T in thinner air, v_i must increase as $1/\sqrt{\rho}$. In this case, as ρ dropped by a factor of 5 to 10 compared to sea level, the required v_i roughly doubled or tripled. The rotor attempts to achieve that by spinning faster. Yet, there are practical limits: the motor can only supply so much torque, and at some point the rotor may reach its RPM limit. The net effect visible, was that the downwash wind speed near the surface did not increase linearly with RPM at low pressure. The rotor was working harder to maintain thrust, rather than to significantly increase the near-ground wind. This is a crucial point when extrapolating to Martian operations: a rotorcraft can hover in thin air, but it produces a more gentle wash relative to the rotor power than it would in dense air. For instance, observers noted that Ingenuity's flights did stir up some dust on Mars, but not massive dust clouds-consistent with the notion that the downwash was just at the threshold of motion. This experiment proved this: at low p, even running the rotor flat-out yielded only in marginal sand movement. From an engineering design perspective, if the aim is to avoid mobilising surface material and mitigate brownout, larger rotors and multi-rotor configurations should be avoided where practicable, since they strengthen near-surface shear and broaden the wall jet. Designs that limit disk loading per footprint, keep greater stand-off from the surface when possible, and use gentle power changes reduce the likelihood of dust lifting.

Another interesting note, is a nearly linear relation between the rotor speed and friction velocity, as can be seen in Figure 5.5. Even with a non-linear increase of RPM per density, the friction velocity does seems to approximate linear behaviour to the rotational velocity of the rotor. This is in agreement with earlier findings of Waza *et al.* (2023).

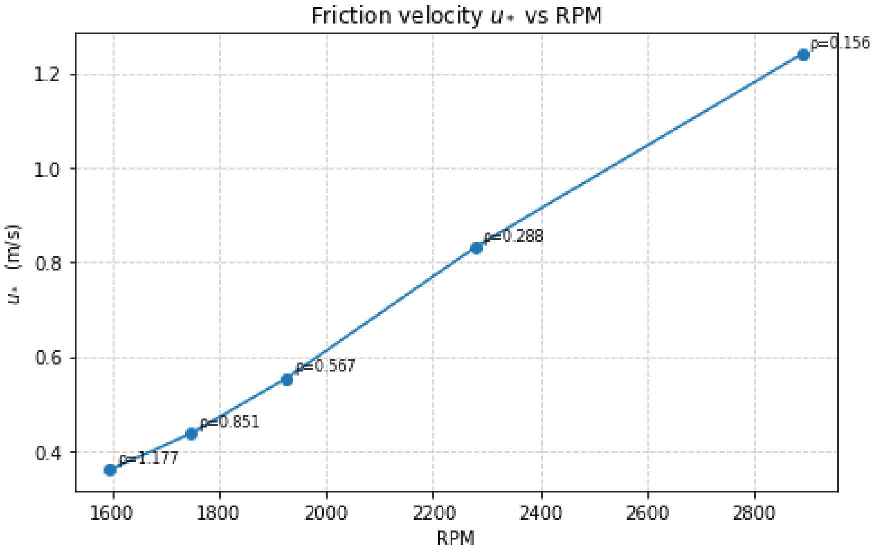

Figure 5.5: Calculated friction velocity u_* vs. RPM for small rotor at h_1, for 200 μm grains. A least-square fit provides a linear trend line: $u_* = 0.0007\omega - 0.7665$, with $R^2 = 0.9982$.

5.8. Thrust Estimation

For this thesis, the thrust has been estimated using the actuator disk model. This first order approximation treats the rotor as an idealized, infinitely thin disk with a uniform pressure jump. It assumes a steady, incompressible flow and neglects complex blade aerodynamics. Some key assumptions and simplifications in the model include:

- The rotor is represented as a uniformly loaded disk (constant thrust distribution), with no discrete blade effects.
- The induced velocity v_i is uniform across the disk area and along the axis of rotation (no radial variation in this simplified model).
- The flow is assumed incompressible and inviscid, and the analysis is steady-state.
- No swirl or rotational components are imparted to the wake (i.e., the model ignores the angular momentum in the wake, which is related to rotor torque).
- Finite rotor blade number, tip losses, and hub drag are not accounted for explicitly.

In reality, helicopter rotors have a non-uniform inflow (more induced velocity in the center, less toward the tips due to tip vortices and finite blade effects), and there are losses near the blade tips and at the hub. Despite these simplifications, the actuator disk model provides a reasonably good first approximation for hover performance. For predicting thrust in hover, it often comes within about 5–15% of experimental measurements for well-designed rotors (Leishman, 2006). The primary sources of error are the neglect of viscous drag distribution, non-uniform inflow, and tip vortex effects, which can slightly reduce efficiency compared to the ideal. Given the lack of detailed rotor performance data for the propeller in thin air, the actuator disk approach was a justified starting point. Still, one must be cautious in over-interpreting the results. For example, the uniform induced flow assumption might misestimate the shear velocity at the ground. In a real rotor flow, there may be a strong outward radial component along the ground (a “wall jet” flow in ground effect (Rabinovitch *et al.*, 2021)), whereas the simple model doesn’t capture that structure. Overall, while the thrust and u_* estimates from the model are useful for discussion, they could be refined with preciser methods.

5.9. Recommendations

Based on the findings and the limitations discussed above, some recommendations are proposed for future work and improvements to the study:

- Apply a more advanced rotor analysis or simulation (*e.g.*, a Blade Element Momentum theory or full CFD model) to better predict the thrust and flow field in low-pressure conditions. This would account for blade aerodynamics, tip losses, and non-uniform inflow, providing more accurate estimates of u_* and rotor performance than the ideal actuator disk model.
- Extend the experiments to even lower pressures (atmospheric densities approximating the Mars 6-10 mbar atmosphere) to investigate whether the threshold friction velocity continues to increase or if it begins to decrease as predicted by Andreotti *et al.* (2021). Testing in this extreme regime would help confirm the existence of the "lower-than-expected" threshold phenomenon and improve the understanding of sediment transport in ultra-thin atmospheres.
- Improve the experimental setup for detecting initial grain motion. For example, use a top-down camera view (looking at the surface from above) instead of or in addition to a side view. An overhead perspective, possibly with proper lighting and high-speed imaging, would make it easier to detect the very onset of particle movement, without interference. This could yield more precise determination of the threshold and allow automated image analysis to quantify motion initiation.

6

Conclusion

The central research question of this thesis was:

> *"How are thresholds and intensity of dust entrainment by rotor downwash modulated across an Earth-to-Martian-like pressure gradient?"*

The experiments performed in a controlled hypobaric environment demonstrated that the threshold friction velocity (u_*) required to initiate particle motion increases as the atmospheric pressure decreases. This finding is consistent with theoretical expectations: as density drops, the rotor must generate higher induced velocities to deliver the same shear stress at the surface. Although lower pressures allowed the rotors to reach higher RPM values due to reduced aerodynamic drag, the decreased mass flux of air limited the maximum shear that could be imposed. Therefore, only fine dust is likely to be mobilised, while coarser grains remain stable even at high rotor speeds.

A further outcome of this thesis is the observation of hysteresis between initiation and sustainment thresholds. The large-rotor experiments revealed that once particles were in motion, lower friction velocities were sufficient to maintain saltation compared to those required to initiate it. This distinction between fluid and impact thresholds confirms a key aspect of aeolian transport theory and highlights the importance of considering both conditions when assessing rotor–surface interactions. In operational contexts, this hysteresis helps to contextualise field reports of localised "sand-blasting" downwind of Ingenuity: once motion is seeded, transport can persist under winds that would not have initiated it from rest.

The results at Earth-ambient pressure aligned with established threshold values for quartz sand, providing verification of the experimental approach. As pressure decreased, thresholds rose linearly (approximately linearly over the tested range), broadly in line with the Shao & Lu and Kok models, although deviations became apparent at the lowest pressures. The experiments did not reach the extremely low-pressure regime where Andreotti *et al.* (2021) reported unexpectedly low thresholds, so no claim is made about that regime here.

Several environmental and surface factors may have influenced thresholds in the lowest-pressure runs. Brief fogging was observed during rapid depressurisation, consistent with transient condensation. Such moisture, together with compaction of the sand bed and possible electrostatic charging, *could* elevate thresholds. These influences were not directly quantified in this study; they are therefore identified as potential contributors and limitations rather than definitive causes.

A study-specific modelling insight concerns the treatment of kinematic viscosity. Analyses that assumed a constant ν diverged from measurements as pressure decreased. Incorporating the pressure dependence of $\nu = \mu/\rho$ (with μ approximately constant over the measured temperature range) brought the Rabinovitch-based u_* predictions closer to the Law-of-Wall and Shao/Kok thresholds. This demonstrates that assuming constant kinematic viscosity under variable density biases threshold estimates at low pressure. Correcting the pressure dependence of ν is a key result of this thesis.

Looking forward, several recommendations of research emerge from this work. Higher-fidelity aerodynamic modelling, through blade-element momentum theory or computational fluid dynamics, could better capture the complex near-ground flow structures (tip-vortex dynamics, swirl, recirculation) that the idealised actuator-disk framework omits. Future experiments should extend to lower pressures approaching 6–10 mbar, with improved imaging and velocimetry to directly measure near-surface shear stresses. Gas composition can be selected based on the experiment's goals: matching ρ and the relevant dimensionless groups can be achieved in either air or CO_2, whereas composition-specific effects should be pursued when those physics are the target. Systematic variation of grain size, density, and controlled moisture content would help isolate surface-property sensitivities, and top-down imaging would enable more precise identification of entrainment onset.

In summary, this thesis demonstrates the strong dependence of rotor-induced dust entrainment on ambient pressure and extends understanding of how thresholds scale across Earth-to-Mars conditions. It confirms the rising difficulty of mobilising surface material in thin atmospheres, shows the presence of hysteresis between initiation and sustainment thresholds, and identifies the pressure dependence of kinematic viscosity as an essential ingredient for modelling thresholds at low pressure. By providing experimental evidence across a wide pressure gradient and comparing the results with theoretical models, the work offers validation and new insights relevant for planetary rotorcraft design and operation, and it lays a foundation for future studies that can refine the physics of dust entrainment under extraterrestrial conditions.

References

Alfaro, S. C., Bouet, C., Khalfallah, B., Shao, Y., Ishizuka, M., Labiadh, M., Marticorena, B., Laurent, B., & Rajot, J. L. (2022). Unraveling the roles of saltation bombardment and atmospheric instability on magnitude and size distribution of dust emission fluxes: Lessons from the JADE and WIND-o-v experiments [Publisher: John Wiley & Sons, Ltd]. *Journal of Geophysical Research: Atmospheres*, *127*(12), e2021JD035983. https://doi.org/10.1029/2021JD035983

Andreotti, B., Claudin, P., Iversen, J. J., Merrison, J. P., & Rasmussen, K. R. (2021). A lower-than-expected saltation threshold at martian pressure and below. *Proceedings of the National Academy of Sciences*, *118*(5), e2012386118. https://doi.org/10.1073/pnas.2012386118

Bagnold, R. A. (1994). The physics of blown sand and desert dunes. london: Methuen. *ResearchGate*. https://doi.org/10.1177/030913339401800105

Balme, M., & Hagermann, A. (2006). Particle lifting at the soil-air interface by atmospheric pressure excursions in dust devils [_eprint: https://onlinelibrary.wiley.com/doi/pdf/10.1029/2006GL026819]. *Geophysical Research Letters*, *33*(19). https://doi.org/10.1029/2006GL026819

Bridges, N. T., Ayoub, F., Avouac, J. P., Leprince, S., & Lucas, A. (2012). Earth-like sand fluxes on mars. *Nature*.

Caprace, D.-G., Baker, E., Diaz, P. V., & Yoon, S. (2024). Comparing planetary helicopter brownout observations with numerical predictions for ingenuity [NTRS Author Affiliations: Oak Ridge Associated Universities, Universities Space Research Association, Science and Technology Corporation (United States), Ames Research Center NTRS Document ID: 20240008174 NTRS Research Center: Ames Research Center (ARC)]. https://ntrs.nasa.gov/citations/20240008174

de Vet, S. J., Merrison, J. P., Mittelmeijer-Hazeleger, M. C., van Loon, E. E., & Cammeraat, L. H. (2014). Effects of rolling on wind-induced detachment thresholds of volcanic glass on mars. *Planetary and Space Science*, *103*, 205–218. https://doi.org/10.1016/j.pss.2014.07.012

Duan, S., Cheng, N., & Xie, L. (2013). A new statistical model for threshold friction velocity of sand particle motion. *CATENA*, *104*, 32–38. https://doi.org/10.1016/j.catena.2012.04.009

Etyemezian, V., Nikolich, G., Ahonen, S., Pitchford, M., Sweeney, M., Purcell, R., Gillies, J., & Kuhns, H. (2007). The portable in situ wind erosion laboratory (PI-SWERL): A new method to measure PM10 windblown dust properties and potential for emissions. *Atmospheric Environment*, *41*(18), 3789–3796. https://doi.org/10.1016/j.atmosenv.2007.01.018

Filippone, A., *et al.* (2019). Rotor wake modelling in ground effect conditions. *45th European Rotorcraft Forum*.

Fisher, A., & Johnson, A. (2024, January 25). *After three years on mars nasas ingenuity helicopter mission ends* [NASA jet propulsion laboratory (JPL)]. https://www.jpl.nasa.gov/news/after-three-years-on-mars-nasas-ingenuity-helicopter-mission-ends/

Gillies, J., Etyemezian, V., Kuhns, H., McAlpine, J., King, J., Uppapalli, S., Nikolich, G., & Engelbrecht, J. (2010). Dust emissions created by low-level rotary-winged aircraft flight over desert surfaces. *Atmospheric Environment*, *44*(8), 1043–1053. https://doi.org/10.1016/j.atmosenv.2009.12.018

Greeley, R., Leach, R., White, B., Iversen, J., & Pollack, J. (1980). Threshold windspeeds for sand on mars: Wind tunnel simulations [_eprint: https://agupubs.onlinelibrary.wiley.com/doi/pdf/10.1029/GL007i002p001 *Geophysical Research Letters*, *7*(2), 121–124. https://doi.org/10.1029/GL007i002p00121

Greeley, R., White, B., Leach, R., Iversen, J., & Pollack, J. (1976). Mars: Wind friction speeds for particle movement [_eprint: https://agupubs.onlinelibrary.wiley.com/doi/pdf/10.1029/GL003i008p00417]. *Geophysical Research Letters*, *3*(8), 417–420. https://doi.org/10.1029/GL003i008p00417

Greeley, R. (2002). Saltation impact as a means for raising dust on mars. *Planetary and Space Science*, *50*(2), 151–155. https://doi.org/10.1016/S0032-0633(01)00127-1

Hamilton, V. E. (2010). Thermal infrared (vibrational) spectroscopy of mg–fe olivines: A review and applications to determining the composition of planetary surfaces. *Geochemistry*, *70*(1), 7–33. https://doi.org/10.1016/j.chemer.2009.12.005

Hébrard, E., Listowski, C., Coll, P., Marticorena, B., Bergametti, G., Määttänen, A., Montmessin, F., & Forget, F. (2012). An aerodynamic roughness length map derived from extended martian rock abundance data [_eprint: https://onlinelibrary.wiley.com/doi/pdf/10.1029/2011JE003942]. *Journal of Geophysical Research: Planets*, *117*. https://doi.org/10.1029/2011JE003942

Hillel, D. (1998, August 31). *Environmental soil physics*. https://shop.elsevier.com/books/environmental-soil-physics/hillel/978-0-12-348525-0

Iversen, J. D., & White, B. R. (1982). Saltation threshold on earth, mars and venus. *Sedimentology*, *29*(1), 111–119. https://doi.org/10.1111/j.1365-3091.1982.tb01713.x

Kok, J. (2010). An improved parameterization of wind□blown sand flux on mars that includes the effect of hysteresis. *Geophysical Research Letters*, *37*(12), 2010GL043646. https://doi.org/10.1029/2010GL043646

Kok, J., Parteli, E. J. R., Michaels, T. I., & Karam, D. B. (2012). The physics of wind-blown sand and dust [Publisher: IOP Publishing]. *Reports on Progress in Physics*, *75*(10), 106901. https://doi.org/10.1088/0034-4885/75/10/106901

Koning, W. J. F., & Dominguez, M. (2024, February 1). *Mars helicopter ingenuity rotor geometry* (NTRS Author Affiliations: Science and Technology Corporation (United States), Ames Research Center NTRS Document ID: 20240001510 NTRS Research Center: Ames Research Center (ARC)). https://ntrs.nasa.gov/citations/20240001510

Leishman, J. G. (2006). *Principles of helicopter aerodynamics*. Cambridge University Press.

Lemmon, M. T., Lorenz, R. D., Rabinovitch, J., Newman, C. E., Williams, N. R., Sullivan, R., Golombek, M. P., Bell, J. F., Maki, J. N., & Vicente□Retortillo, A. (2022). Lifting and transport of martian dust by the ingenuity helicopter rotor downwash as observed by high□speed imaging from the perseverance rover. *Journal of Geophysical Research: Planets*, *127*(12), e2022JE007605. https://doi.org/10.1029/2022JE007605

Li, X., & Zhang, H. (2011). Research on threshold friction velocities during dust events over the gobi desert in northwest china [_eprint: https://onlinelibrary.wiley.com/doi/pdf/10.1029/2010JD015572]. *Journal of Geophysical Research: Atmospheres*, *116*. https://doi.org/10.1029/2010JD015572

Logreira, D. (2023, June 15). *Mars sample return - NASA science* [Running Time: 49 Section: Mars Sample Return (MSR)]. https://science.nasa.gov/mission/mars-sample-return/

Lorenz, R. D. (2012). Power law distribution of pressure drops in dust devils: Observation techniques and earth–mars comparison. *Planetary and Space Science*, *60*(1), 370–375. https://doi.org/10.1016/j.pss.2011.11.003

Mahaffy, P. R., Benna, M., Elrod, M., Yelle, R. V., Bougher, S. W., Stone, S. W., & Jakosky, B. M. (2015). Structure and composition of the neutral upper atmosphere of mars from the MAVEN NGIMS investigation. *Geophysical Research Letters*, *42*(21), 8951–8957. https://doi.org/10.1002/2015GL065329

Merrison, J. P., Bechtold, H., Gunnlaugsson, H., Jensen, A., Kinch, K., Nornberg, P., & Rasmussen, K. (2008). An environmental simulation wind tunnel for studying aeolian transport on mars. *Planetary and Space Science*, *56*(3), 426–437. https://doi.org/10.1016/j.pss.2007.11.007

Merrison, J., Gunnlaugsson, H., Nørnberg, P., Jensen, A., & Rasmussen, K. (2007). Determination of the wind induced detachment threshold for granular material on mars using wind tunnel simulations. *Icarus*, *191*(2), 568–580. https://doi.org/10.1016/j.icarus.2007.04.035

Modesto, M. (2017). Beating brownout - joint air power competence centre. *The Journal of the JAPCC*, (24). https://www.japcc.org/articles/beating-brownout/

NASA. (2019). NASA's dragonfly will fly around titan looking for origins, signs of life.

NASA. (2025). *Propeller thrust*. Retrieved October 8, 2025, from https://www.grc.nasa.gov/WWW/K-12/airplane/propth.html

NATO. (2012). *Rotary-wing brownout mitigation: Technologies and training* [NATO science and technology organization]. Retrieved September 30, 2025, from https://www.sto.nato.int/document/rotary-wing-brownout-mitigation-technologies-and-training/

NOAA. (2024). *The atmosphere | national oceanic and atmospheric administration*. https://www.noaa.gov/jetstream/atmosphere

Perko, H. A., Nelson, J. D., & Green, J. R. (2002, June). *Review of martian dust: Composition, transport, deposition, adhesion and removal* [ResearchGate]. https://www.researchgate.net/publication/252484582_Review_of_Martian_Dust_Composition_Transport_Deposition_Adhesion_and_Removal

Phillips, C., & Brown, R. E. (2008). The effect of helicopter configuration on the fluid dynamics of brownout [Num Pages: 704756]. *34th European Rotorcraft Forum*. https://strathprints.strath.ac.uk/27434/

Phillips, C., Kim, H. W., & Brown, R. E. (2010). The flow physics of helicopter brownout [Num Pages: 3041506]. *66th American Helicopter Society Forum: Rising to New Heights in Vertical Lift Technology*. https://strathprints.strath.ac.uk/27362/

Rabinovitch, J., Lorenz, R., Slimko, E., & Wang, K.-S. C. (2021). Scaling sediment mobilization beneath rotorcraft for titan and mars. *Aeolian Research*, *48*, 100653. https://doi.org/10.1016/j.aeolia.2020.100653

Shao, Y., & Klose, M. (2016). A note on the stochastic nature of particle cohesive force and implications to threshold friction velocity for aerodynamic dust entrainment. *Aeolian Research*, *22*, 123–125. https://doi.org/10.1016/j.aeolia.2016.08.004

Shao, Y., & Lu, H. (2000). A simple expression for wind erosion threshold friction velocity. *Journal of Geophysical Research: Atmospheres*, *105*, 22437–22443. https://doi.org/10.1029/2000JD900304

Southard, J. (2019, April 22). *Introduction to fluid motions and sediment transport (southard)* [Geosciences LibreTexts]. https://geo.libretexts.org/Bookshelves/Sedimentology/Introduction_to_Fluid_Motions_and_Sediment_Transport_(Southard)

Sullivan, R., Arvidson, R., Bell, J. F., Gellert, R., Golombek, M., Greeley, R., Herkenhoff, K., Johnson, J., Thompson, S., Whelley, P., & Wray, J. (2008). Wind□driven particle mobility on mars: Insights from mars exploration rover observations at “el dorado” and surroundings at gusev crater. *Journal of Geophysical Research: Planets*, *113*, 2008JE003101. https://doi.org/10.1029/2008JE003101

Sullivan, R., & Kok, J. F. (2017). Aeolian saltation on mars at low wind speeds. *Journal of Geophysical Research: Planets*, *122*(10), 2111–2143. https://doi.org/10.1002/2017JE005275

Swann, C., Sherman, D. J., & Ewing, R. C. (2020). Experimentally derived thresholds for windblown sand on mars. *Geophysical Research Letters*, *47*(3), e2019GL084484. https://doi.org/10.1029/2019GL084484

Sweeney, M. R. (2022, January 1). 7.10 - dust emission processes. In J. (F. Shroder (Ed.), *Treatise on geomorphology (second edition)* (pp. 235–258). Academic Press. https://doi.org/10.1016/B978-0-12-818234-5.00015-8

Tarot. (2025). *TSERIES1155 CARBON FIBER PROPELLER CW/CCW TL2827*. Retrieved October 8, 2025, from http://www.tarotrc.com/Product/Detail.aspx?Lang=en&Id=5f39d4c9-e14f-4aac-8c86-5e0158ed28be

Technologies, S. R. (2025). *Mars global (MGS-1) high-fidelity martian regolith simulant* [Space resource technologies]. Retrieved October 8, 2025, from https://spaceresourcetech.com/products/mgs-1-mars-global-simulant

Tmotor. (2025a). *FA26.2*8.5 prop-2pcs/PAIR_uav folding propellers_uav carbon fiber propellers_multi-rotor UAV propellers_multi-rotor UAV power_t-motor store | UAV & FPV drone motors, ESCs, propellers* [T-motor]. Retrieved October 8, 2025, from https://store.tmotor.com/product/folding-carbon-fiber-26_2x8_5-prop.html

Tmotor. (2025b). *U8 lite KV150 multi-rotor motor for industrial applications* [T-motor]. Retrieved October 8, 2025, from https://store.tmotor.com/product/u8-lite-u-efficiency-kv150.html

van der Voort, R. M., de Lint, J. A., Mingelen, C., Grootes, O. C. B., Oostwoud, F. T. W., Derie, C. J. T., Paddeu, J., Masure, K. R. G., Van der Straeten, M., & Wennink, T. S. (2022). Kite power for an electric pickup truck. Retrieved October 8, 2025, from https://repository.tudelft.nl/record/uuid:62110ec4-d06f-4d3f-b590-019a213ade59

Van Leeuwen, C., Fister, W., Vos, H., Cammeraat, L., & Kuhn, N. (2021). A cross-comparison of threshold friction velocities for PM10 emissions between a traditional portable straight-line wind tunnel and PI-SWERL. *Aeolian Research*, *49*, 100661. https://doi.org/10.1016/j.aeolia.2020.100661

Ventura Diaz, P., & Caprace, D.-G. (2024). *Decoding martian dust: Brownout simulations of the ingenuity mars helicopte* [NASA@SC24]. https://www.nas.nasa.gov/SC24/research/project06.php

Wadcock, A. J., Ewing, L. A., Solis, E., Potsdam, M., & Rajagopalan, G. (2008). Rotorcraft downwash flow field study to understand the aerodynamics of helicopter brownout. https://apps.dtic.mil/sti/html/tr/ADA509010/index.html

Wang, L., Li, C., Lin, J., & Ni, S. (2023). Development of an intelligent wind erosion monitoring system. *Sensors (Basel, Switzerland)*, *23*(23), 9389. https://doi.org/10.3390/s23239389

Warmbrodt, W. (2025, October 1). *Helicopter brownout research*. https://rotorcraft.arc.nasa.gov/Research/Programs/brownout.html

Waza, A., Kjer, J., Peiteado, M., Jardiel, T., Iversen, J., Rasmussen, K., & Merrison, J. (2023). Aeolian dust resuspension on mars studied using a recirculating environmental wind tunnel. *Planetary and Space Science*, *227*, 105638. https://doi.org/10.1016/j.pss.2023.105638

White, B. R. (1979). Soil transport by winds on mars [NTRS Author Affiliations: California, University NTRS Document ID: 19790064513 NTRS Research Center: Legacy CDMS (CDMS)]. *Journal of Geophysical Research*, *84*. https://ntrs.nasa.gov/citations/19790064513

White, B. R., Greeley, R., & Leach, R. N. (1991). Martian dust threshold measurements: Simulations under heated surface conditions [NTRS Author Affiliations: California Univ., Arizona State Univ. NTRS Document ID: 19910017767 NTRS Research Center: Legacy CDMS (CDMS)]. https://ntrs.nasa.gov/citations/19910017767

White, F. (2016). *Fluid mechanics (8th edition) in SI units | PDF | fluid dynamics | compressible flow* [Scribd]. Retrieved October 2, 2025, from https://www.scribd.com/document/906990402/Fluid-Mechanics-8th-Edition-in-SI-Units

Williams, D. R. (2025, May 19). *Mars fact sheet* [NASA]. https://nssdc.gsfc.nasa.gov/planetary/factsheet/marsfact.html

Wolf, C., Schwarz, C., Kaufmann, K., Gardner, A., Michaelis, D., Bosbach, J., Schanz, D., & Schröder, A. (2022). Experimental study of secondary vortex structures in a rotor wake. *Proceedings of the European Rotorcraft Forum*.

Yamauchi, G., & Ramasamy, M. (2017). Using model-scale tandem-rotor measurements in ground effect to understand full-scale ch-47d outwash. *Journal of the American Helicopter Society*, *62*(1), 1–13.

Zafiropoulos, A. (2025). Preferred grain orientation quantification in mars analogue conditions using wind tunnel experiments. Retrieved October 8, 2025, from https://repository.tudelft.nl/record/uuid:9705b646-cc82-4a8a-8d97-3aaeb9e9f736

Zhang, J., Li, G., Shi, L., Huang, N., & Shao, Y. (2022, March 17). Impact of turbulence on aeolian sand and dust entrainment: Results from wind-tunnel experiment. https://doi.org/10.5194/acp-2022-76

Zhang, Y., Gillebaart, T., Van Zuijlen, A., Van Bussel, G., & Bijl, H. (2017). Experimental and numerical investigations of aerodynamic loads and 3d flow over non□rotating MEXICO blades. *Wind Energy*, *20*(4), 585–600. https://doi.org/10.1002/we.2025

A

Models Comparison

This appendix contains an overview of the models discussed in Chapter 2. It includes the model's origin, application, in- and output parameters, assumption and validations.

Table A.1: Comparison of Dust Lofting and Saltation Models for Mars (part 1)

Model (Year)	**Origin & Application**	**Key Input Parameters**	**Key Outputs**	**Underlying Assumptions**	**Validation / Notes**
Rabinovitch et al. (2021)	Developed during Mars Ingenuity design; predicts dust lofting under rotor downwash on Mars (and Titan)	rotorcraft thrust/weight, rotor size & RPM, height above ground, atmospheric density (planet gravity indirectly)	Surface friction velocity as function of rotor height; analytical threshold prediction (yes/no dust)	Steady, axisymmetric rotor flow (wall-jet + tip vortices); constant descent or hover; ignores complex transients and terrain effects	Partially validated with Ingenuity 2021 flights. Correctly anticipated dust occurrence and order-of-magnitude u^*, but underestimates dust lifting at higher altitudes. Useful for quick scaling across planets, but needs refinements for unsteady and lateral effects.
Andreotti et al. (2021)	Laboratory wind tunnel experiments at low pressure; explores fundamental aeolian transport on Mars	Air pressure (0.01-1 bar range), grain size & density, wind shear velocity (controlled in tunnel)	Threshold wind speed for saltation onset; saltation regime characteristics (e.g., ripple wavelength)	Steady uniform wind; homogeneous sand bed; closed system (no abrasive dust influx); cohesion of grains similar to Earth analogue	Validated in lab (PNAS study). Revealed regime threshold drops at Martian pressures. Not yet validated directly on Mars, but provides useful analogues for exploration of surface wind motion. Suggests collective grain effects dominate at low pressure.
Lemmon et al. (2022) - Ingenuity flight data analysis	Field observation (Jezero crater, Mars) using Perseverance rover imagery; measures actual dust clouds from rotorcraft	Video derived dust cloud size, density & motion; Ingenuity telemetry (altitude, etc.); uses Rabinovitch model and known env. conditions (pressure 7 mbar)	Estimated dust mass lifted per flight; deduced wind speeds/ friction velocity causing dust; qualitative dust dispersion patterns	Assumes video brightness correlates to dust mass; uses analytical model to invert observations (assuming threshold concept holds); dust optical properties need estimation	*in-situ* validation dataset. Found 1.8 g of dust lofted per 1.8 kg rotorcraft (0.1%); threshold $v_* 0.5$ m/s for dust on Mars; dust seen up to 5-6 m altitude. Good agreement with models on low threshold, but indicates dust aggregates can be lifted without full saltation. Limited to one locale and vehicle.

Table A.2: Comparison of Dust Lofting and Saltation Models for Mars (part 2)

Model (Year)	Origin & Application	Key Input Parameters	Key Outputs	Underlying Assumptions	Validation / Notes
Shao & Lu (2000) - Classical (Earth)	Theoretical / empirical model for wind erosion initiation on Earth; widely used in dust models (e.g., climate simulations)	Grain diameter (for ideal dry sand); air density; empirical constants for drag, lift, cohesion	Threshold friction velocity v_{*t} as function of grain size; explains min. threshold at 100 μm and increase for finer/coarser grains	Spherical grains loosely on surface; steady turbulent flow; no saltation feedback (static initiation); cohesion linear with diameter; Earth gravity/air by default	Validated for Earth sands (alb/field). Forms basis of many dust emission schemes. Overestimates Martian threshold if unmodified - doesn't include low pressure effects or impact creep. Needs adjustment (e.g., lower cohesion or added mechanisms) for Mars use.
Swann et al. (2020) - Mars threshold wind tunnel	Experimental threshold determination in NASA Ames Mars Wind Tunnel (MARSWIT); Mars analogue testing	Atmospheric pressure (Martian 7 mbar vs Earth 1 bar); grain size 100-150 μm; wind speed increased until motion observed	Threshold shear velocity for sand movement (both initial fluid threshold and sustained impact threshold); observed mode of particle motion (sporadic vs continuous)	Defines threshold at first grain motion (very intermittent); controlled lab conditions with Mars-like CO2 atmosphere; assumes similar grain cohesion as Earth analogue soils	Consistent with Andreotti 2021: found previous models too high by 1.6-2.5x. Indicates fluid threshold on Mars 0.7-1.0 m/s, but lower motion starts at lower v_{*t}. Provides empirical Mars-specific threshold for use in models (e.g., used in Lemmon 2022). Limited by short test duration and specific sand type.
CFD Rotorcraft Dust Models (e.g., Caprace et al. 2024)	Numerical simulation of rotor airflow and dust pickup; applied to Ingenuity scenario and future rotorcraft	Rotor geometry and flight parameters; atmospheric properties; sediment bed properties (threshold v_*^t, dust flux efficiency, etc. as submodels)	Detailed flow field (velocity, vortices); wall shear stress distribution; predicted dust concentration and total lifted mass	Assumes correct turbulence modelling (e.g., k-ϵ or LES); requires empirical dust uplift coefficients; high computational cost limits parameter sweeps	Qualitative validation with Ingenuity data: captures dust cloud presence and some features. Indicates rotor influence > expected at height (shallower decay of v_*). Outcome sensitive to input threshold and efficiency parameters - highlights need for accurate Mars soil properties. Promising for design predictions (e.g., Mars Sample Return helis, Dragonfly), once calibrated.

B

Collected Data

This appendix contains all the measured and calculated datapoints.

Table B.1: Threshold friction velocity from Shao & Lu and Kok formulations for different particle diameters

Particle diameter (μm)	Density (kg/m^3)	Shao & Lu (u_{*t} m/s)	Kok (fluid) (u_{*t} m/s)	Kok (impact) (u_{*t} m/s)
50	1.177	0.2762	0.1051	0.0862
50	0.851	0.3248	0.1236	0.1013
50	0.567	0.3981	0.1515	0.1242
50	0.288	0.5580	0.2123	0.1741
50	0.156	0.7589	0.2887	0.2368
50	0.095	0.9722	0.3699	0.3033
200	1.177	0.2646	0.2101	0.1723
200	0.851	0.3112	0.2471	0.2027
200	0.567	0.3814	0.3029	0.2484
200	0.288	0.5345	0.4246	0.3481
200	0.156	0.7270	0.5775	0.4735
200	0.095	0.9313	0.7398	0.6066
500	1.177	0.3770	0.3323	0.2725
500	0.851	0.4433	0.3908	0.3204
500	0.567	0.5434	0.4790	0.3927
500	0.288	0.7615	0.6713	0.5505
500	0.156	1.0358	0.9131	0.7487
500	0.095	1.3269	1.1697	0.9592

C

Code: Shao & Lu, and Kok et al.

This is the Python script for establishing the threshold friction velocity, using both the model of Shao & Lu, as well as the model by Kok et al..

```python
# -*- coding: utf-8 -*-
"""
Combined␣plot:␣Shao␣&␣Lu␣vs␣Kok␣et␣al.␣threshold␣friction␣velocity␣(u*)
"""

import numpy as np
import matplotlib.pyplot as plt

# ---------- Shared inputs ----------
g = 9.81                  # m/s^2
density_p = 2650          # kg/m^3 (particle density)
d_values = [50e-6, 200e-6, 500e-6]                    # particle diameters

# density_air_values = [1.1768, 0.851, 0.5665, 0.2884, 0.156, 0.095]  # kg/m^3, smallprop @ h1
density_air_values = [1.1768, 0.851, 0.5665, 0.2884, 0.212, 0.095]  # kg/m^3, smallprop @ h2

# ---------- Shao & Lu parameters ----------
A_N = 0.0123
gamma = 3e-4  # N/m

def ustar_shao_lu(d, rho):
    sigma_p = density_p / rho
    return np.sqrt(A_N * (sigma_p * g * d + gamma / (rho * d)))

# ---------- Kok et al. parameters ----------
A_ft = 0.10  # (use 0.082 for impact threshold variant)

def ustar_kok(d, rho):
    return A_ft * np.sqrt(((density_p - rho) / rho) * g * d)

# ---------- Kok et al. parameters ----------
A_it = 0.082  # (use 0.082 for impact threshold variant)

def ustarimpact_kok(d, rho):
    return A_it * np.sqrt(((density_p - rho) / rho) * g * d)

# ---------- Plot ----------
plt.figure(figsize=(8,6))
colors = plt.cm.tab10.colors

for i, d in enumerate(d_values):
    color = colors[i % len(colors)]

    u_shao = []
    u_kok = []
```

```
    u_kok_impact = []

    print(f"\n---␣Particle␣diameter:␣{int(d*1e6)}␣µm␣---")
    for rho in density_air_values:
        val_shao = ustar_shao_lu(d, rho)
        val_kok = ustar_kok(d, rho)
        val_kok_impact = ustarimpact_kok(d, rho)
        u_shao.append(val_shao)
        u_kok.append(val_kok)
        u_kok_impact.append(val_kok_impact)

        # print formatted values
        print(f" ␣=␣{rho:.3f}␣kg/m³␣|␣Shao␣&␣Lu:␣{val_shao:.4f}␣m/s␣|␣Kok:␣{val_kok:.4f}␣m/s␣|␣Kok␣impact:␣{val_kok_impact:.4f}␣m/s")

    # plot Shao & Lu → squares
    plt.plot(u_shao, density_air_values, marker='s', linestyle='-',
             color=color, label=f"Shao␣&␣Lu␣-␣d␣=␣{int(d*1e6)}␣µm")

    # plot Kok et al. → dots
    plt.plot(u_kok, density_air_values, marker='o', linestyle='--',
             color=color, label=f"Kok␣et␣al.␣-␣d␣=␣{int(d*1e6)}␣µm")

plt.ylabel("Air␣density␣(kg/m³)")
plt.xlabel("Threshold␣friction␣velocity␣␣u *␣␣(m/s)")
plt.title("Threshold␣friction␣velocity␣vs␣air␣density")
plt.legend()
plt.grid(True)
plt.tight_layout()
plt.show()
```

D

Code: Law of Wall

This is Python script for the Law of Wall.

```python
# -*- coding: utf-8 -*-
"""
Law␣of␣Wall:␣Plot␣u*␣over␣air␣density␣ ␣for␣different␣surface␣roughness␣z0
"""

import matplotlib.pyplot as plt
import numpy as np

# constants
Karman_cons = 0.41
z = 0.005       # m, height of measurements above ground

# measured wind speeds (same order as rho_values)
u_z_values = [3.0115, 3.19675, 3.41905, 3.86365, 4.5676, 4.4676]  # m/s

# air densities corresponding to each case
rho_values = [1.1768, 0.8510, 0.5665, 0.2884, 0.1559, 0.095]  # kg/m³

# different surface roughness lengths to compare
z0_values = [1.67e-6, 6.67e-6, 1.67e-5]

plt.figure(figsize=(8,6))

for z0 in z0_values:
    u_star_values = []
    for rho, u_z in zip(rho_values, u_z_values):
        u_star = u_z * Karman_cons / (np.log(z / z0))
        u_star_values.append(u_star)
        print(f"z0={z0:.2e}␣|␣ ={rho:.3f}␣kg/m³␣|␣u(z)={u_z:.3f}␣m/s␣-->␣u*={u_star:.3f}␣m/s"
            )

    # plot this z0 curve
    plt.plot(u_star_values, rho_values, marker='o', linestyle='-',
             label=f"d␣=␣{z0:.2e}␣m")

plt.ylabel("Air␣density␣ ␣(kg/m³)")
plt.xlabel("Friction␣velocity␣u*␣(m/s)")
plt.title("Air␣density␣vs␣Friction␣velocity␣using␣Law␣of␣Wall")
plt.legend()
plt.grid(True)
plt.tight_layout()
plt.show()
```

E

Code: Rabinovitch

This is a simplified actuator disk model script (originally done in Excel), followed by the Rabinovitch model script written for the small propeller at h_1.

```python
# -*- coding: utf-8 -*-
"""
Created␣on␣Thu␣Sep␣18␣13:51:58␣2025

@author:␣rmvdv

ACTUATOR␣DISK␣MODEL
"""


#import math
from math import pi
import matplotlib.pyplot as plt
import numpy as np

R = 0.175 # m, small prop
p = 100550 # Pa
R_air = 287.05 # J/(kg*K) for air
Temp = 23.5 + 274.15 # K
u_z = 1.8976 # m/s

rho = p / (R_air*Temp)
A_prop = np.pi * R**2
delta_p = 0.5 * rho*(u_z)**2
thrust = A_prop * delta_p
print(rho,thrust)
```

```python
# -*- coding: utf-8 -*-
"""
RABINOVITCH␣MODEL␣-␣batch␣over␣(density,␣T,␣RPM)␣rows
"""
from math import pi
import numpy as np
import matplotlib.pyplot as plt


# ---------- CONSTANTS (unchanged) ----------
alpha_L = 1.25643        # ’Lambs constant
boundary_phi = 1.31

# Fluid & environmental
dyn_visco = 1.96e-5      # dynamic viscosity (Pa·s)

g = 9.81                 # gravity (m/s^2)
d_p_180 = 1e-6           # particle diameter (m) 180 micrometer
d_p_250 = 250e-6         # particle diameter (m) 250 micrometer
```

```
d_p_500 = 500e-6
rho_p = 2650             # particle density (kg/m^3)

# Rotor & Aerodynamic
D = 0.35                 # rotor diameter (m)
AR = 7
N_blades = 2             # number of blades
h_rotor = 0.175          # rotor-plane height (m)

# Conversions independent of the row
R = D / 2
r = R                    # see section 3.1 after eq. 3, r = R
A = pi * R**2            # rotor area (m²)
c = R / AR               # chord length (m)
rot_solidity = N_blades * c / (pi * R)

# ---------- CORE CALC ----------
def compute_row(density: float, T: float, RPM: float):
    """
␣␣␣␣Returns␣a␣dict␣with␣key␣outputs␣for␣one␣(density,␣T,␣RPM)␣combination.
␣␣␣␣"""
    # Derived fluid property
    # kin_visco = dyn_visco / density
    kin_visco = 1.6e-5

    # Rotor kinematics
    rot_ang_velo = 2 * pi * RPM / 60.0             # rad/s
    tip_speed = rot_ang_velo * R

    # Aerodynamic params
    DL = T / A                                     # disk loading
    C_T = T / (density * pi * (rot_ang_velo**2) * (R**4))
    tip_vortex_circ = 2.3 * C_T * rot_ang_velo * R * c / rot_solidity

    # Stagnation point flow model
    w = 2*np.sqrt(T / (2 * density * A))
    v_vortex = 2.3 / (0.1 * pi) * T / (rot_solidity * density * A * rot_ang_velo * D)
    a = (w + v_vortex) / (2 * h_rotor)

    # Shear & threshold
    shear_wall = dyn_visco * (r) * a**(3/2) * kin_visco**(-1/2) * boundary_phi
    u_star = np.sqrt(shear_wall / density)

    # For sanity check with Table 3
    ratio = v_vortex / w if w != 0 else float("nan")

    return dict(
        density=density,
        T=T,
        RPM=RPM,
        kin_visco=kin_visco,
        tip_speed=tip_speed,
        DL=DL,
        C_T=C_T,
        tip_vortex_circ=tip_vortex_circ,
        v_vortex=v_vortex,
        w=w,
        ratio=ratio,
        shear_wall=shear_wall,
        u_star=u_star,
    )

# ---------- DATASET ----------
# Fill in measured data:
data = [
    {"density": 1.176843294, "T": 0.513497309301531, "RPM": 1596},
    {"density": 0.851012044, "T": 0.41835299473667, "RPM": 1746},
    {"density": 0.566538578, "T": 0.318852581278915, "RPM": 1926},
    {"density": 0.288412487, "T": 0.206815944429116, "RPM": 2278},
    {"density": 0.155863883, "T": 0.156565727856233, "RPM": 2889},
    {"density": 0.094800000, "T": 0.0923016454604824, "RPM": 2900},
```

```python
]

# Lower windspeed
# data = [
#     {"density": 1.176843294, "T": 0.229093, "RPM": 1596},
#     {"density": 0.851012044, "T": 0.197554, "RPM": 1746},
#     {"density": 0.566538578, "T": 0.159613, "RPM": 1926},
#     {"density": 0.288412487, "T": 0.113613, "RPM": 2278},
#     {"density": 0.155863883, "T": 0.095515, "RPM": 2889},
#     {"density": 0.094800000, "T": 0.054256, "RPM": 2900},
# ]

# Data if reverse engineering from Shao et al & Kok et al
# data = [
#     {"density": 1.176843294, "T": 0.183, "RPM": 1596},
#     {"density": 0.851012044, "T": 0.183, "RPM": 1746},
#     {"density": 0.566538578, "T": 0.183, "RPM": 1925},
#     {"density": 0.288412487, "T": 0.183, "RPM": 2278},
#     {"density": 0.155863883, "T": 0.183, "RPM": 2889},
# ]

# ---------- RUN & PRINT ----------
def fmt(x, digits=5):
    if isinstance(x, (int, np.integer)):
        return str(x)
    if isinstance(x, float) or isinstance(x, np.floating):
        # switch to scientific if very small/large
        return f"{x:.{digits}g}"
    return str(x)

results = [compute_row(row["density"], row["T"], row["RPM"]) for row in data]

# Only print u_star values
# print("u* values (m/s):")
# for r in results:
#     print(f"{r['u_star']:.5f}")



# Columns
cols = [
    "density", "T", "RPM",
    "kin_visco", "tip_speed", "DL", "C_T",
    "v_vortex", "w", "ratio",
    "shear_wall", "u_star"
]

# Compute column widths
col_widths = {k: max(len(k), *(len(fmt(r[k])) for r in results)) for k in cols}
header = "␣|␣".join(k.ljust(col_widths[k]) for k in cols)
sep    = "-+-".join("-" * col_widths[k] for k in cols)
print(header)
print(sep)
for r in results:
    print("␣|␣".join(fmt(r[k]).ljust(col_widths[k]) for k in cols))

# ---------- PLOT u* vs RPM ----------
# Sort by RPM for a clean line plot
results_sorted = sorted(results, key=lambda r: r["RPM"])
rpms   = [r["RPM"] for r in results_sorted]
u_stars = [r["u_star"] for r in results_sorted]
shear_walls = [r["shear_wall"] for r in results_sorted]

plt.figure(figsize=(7, 4.5))
plt.plot(rpms, u_stars, marker="o", linewidth=1.5)
# Optional: label each point with density for reference
for r in results_sorted:
    plt.annotate(f'ρ={r["density"]:.3f}', (r["RPM"], r["u_star"]), xytext=(4, 4), textcoords="offset␣points", fontsize=8)

plt.title(r"Friction␣velocity␣$u_*$␣vs␣RPM")
```

```
plt.xlabel("RPM")
plt.ylabel(r"$u_*$␣␣(m/s)")
plt.grid(True, linestyle="--", alpha=0.6)
plt.tight_layout()
plt.savefig("u_star_vs_rpm.png", dpi=200)
plt.show()
print("\nSaved␣figure:␣u_star_vs_rpm.png")

# ---------- PLOT shear_wall vs d_p_250 ----------
# Each dataset point has same d_p_250, so x will be a constant array
d_p_value = d_p_250
x_vals = [d_p_value for _ in results]
y_vals = [r["shear_wall"] for r in results]

plt.figure(figsize=(6, 4.5))
plt.scatter(x_vals, y_vals, color="crimson", marker="o", s=60, label="shear_wall")
for i, r in enumerate(results):
    plt.annotate(f' ={r["density"]:.3f}', (x_vals[i], y_vals[i]),
                  xytext=(6, 4), textcoords="offset␣points", fontsize=8)

plt.title(r"Shear␣stress␣vs␣particle␣diameter␣$d_p$")
plt.xlabel(r"Particle␣diameter␣$d_p$␣(m)")
plt.ylabel(r"Shear␣stress␣$\tau$␣(Pa)")
plt.yscale("log")  # logarithmic y-axis
plt.ylim(0.01, 1.0)
plt.grid(True, which="both", linestyle="--", alpha=0.6)
plt.tight_layout()
plt.savefig("shear_vs_dp.png", dpi=200)
plt.show()
print("\nSaved␣figure:␣shear_vs_dp.png")

# ---------- PLOT u_star vs d_p_250 ----------
# Each dataset point has same d_p_250, so x will be a constant array
d_p_value = d_p_250
x_vals = [d_p_value for _ in results]
y_vals = [r["u_star"] for r in results]

plt.figure(figsize=(6, 4.5))
plt.scatter(x_vals, y_vals, color="crimson", marker="o", s=60, label="shear_wall")
for i, r in enumerate(results):
    plt.annotate(f' ={r["density"]:.3f}', (x_vals[i], y_vals[i]),
                  xytext=(6, 4), textcoords="offset␣points", fontsize=8)

plt.title(r"u_star␣vs␣particle␣diameter␣$d_p$")
plt.xlabel(r"Particle␣diameter␣$d_p$␣(m)")
plt.ylabel(r"u_star␣$\tau$␣(Pa)")
plt.grid(True, which="both", linestyle="--", alpha=0.6)
plt.tight_layout()
plt.savefig("ustar_vs_dp.png", dpi=200)
plt.show()
print("\nSaved␣figure:␣ustar_vs_dp.png")

# ---------- NEW: PLOT u* vs density ----------
results_sorted_rho = sorted(results, key=lambda r: r["density"])
rhos     = [r["density"] for r in results_sorted_rho]
u_stars2 = [r["u_star"]  for r in results_sorted_rho]

# plt.figure(figsize=(7, 4.5))
plt.plot(u_stars2, rhos, marker="o", linewidth=1.5)
# for r in results_sorted_rho:
#     plt.annotate(f'RPM={r["RPM"]:.0f}', (r["density"], r["u_star"]),
#                    xytext=(4, 4), textcoords="offset points", fontsize=8)
plt.title("Friction␣velocity␣vs␣Air␣density␣using␣the␣Rabinovitch␣model")
plt.ylabel("Air␣density␣ ␣(kg/m³)")
plt.xlabel("Friction␣velocity␣u*␣(m/s)")
plt.grid(True)
plt.tight_layout()
plt.show()
```

F

Gantt Chart

Below is the Gantt chart with the planning for the thesis period.

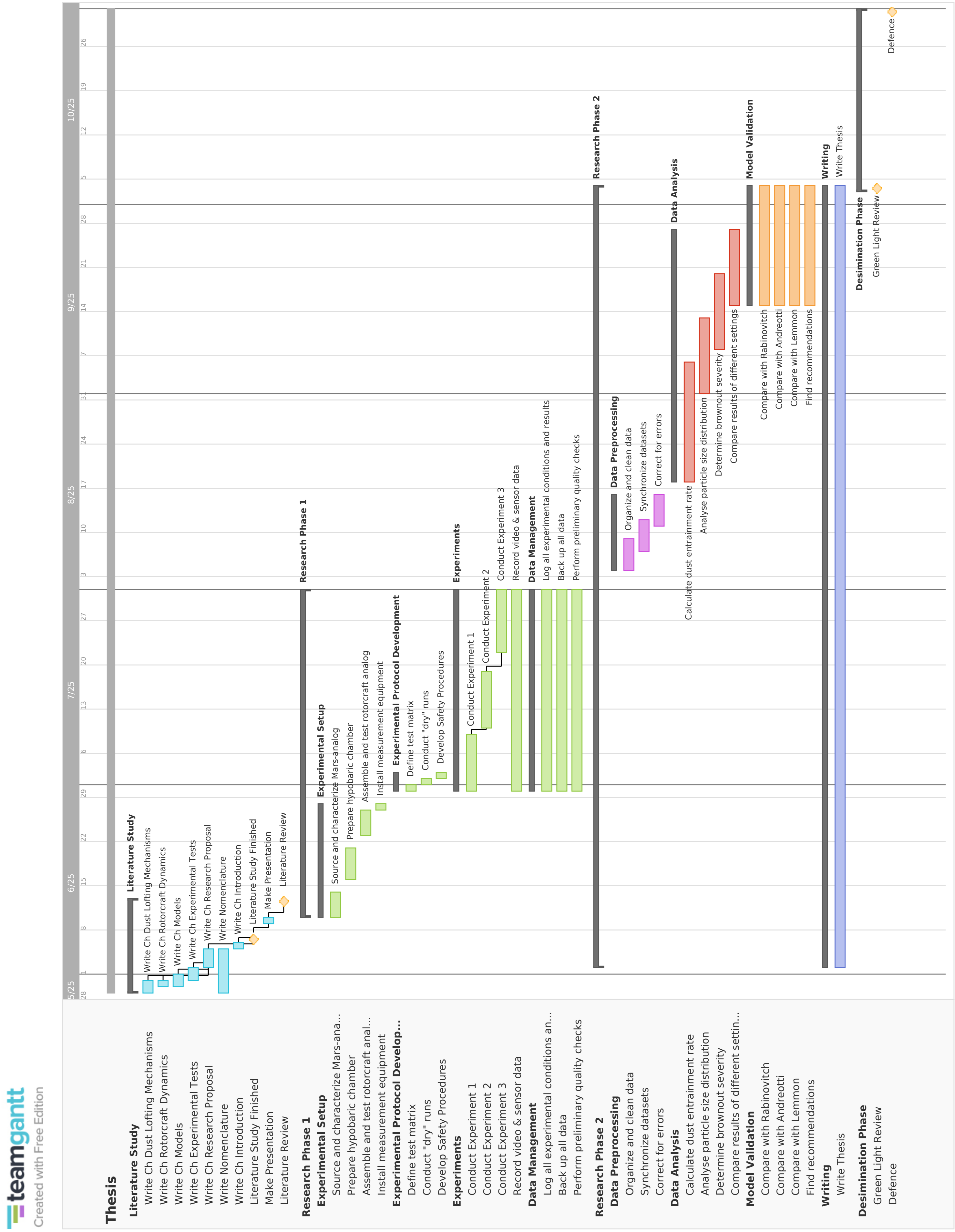
teamgantt
Created with Free Edition
5/25
6/25
7/25
8/25
9/25
10/25
28
1
8
15
22
29
6
13
20
27
3
10
17
24
31
7
14
21
28
5
12
19
26
Thesis
Literature Study
Write Ch Dust Lofting Mechanisms
Write Ch Rotorcraft Dynamics
Write Ch Models
Write Ch Experimental Tests
Write Ch Research Proposal
Write Nomenclature
Write Ch Introduction
Literature Study Finished
Make Presentation
Literature Review
Research Phase 1
Experimental Setup
Source and characterize Mars-ana...
Prepare hypobaric chamber
Assemble and test rotorcraft anal...
Install measurement equipment
Experimental Protocol Develop...
Define test matrix
Conduct "dry" runs
Develop Safety Procedures
Experiments
Conduct Experiment 1
Conduct Experiment 2
Conduct Experiment 3
Record video & sensor data
Data Management
Log all experimental conditions an...
Back up all data
Perform preliminary quality checks
Research Phase 2
Data Preprocessing
Organize and clean data
Synchronize datasets
Correct for errors
Data Analysis
Calculate dust entrainment rate
Analyse particle size distribution
Determine brownout severity
Compare results of different settin...
Model Validation
Compare with Rabinovitch
Compare with Andreotti
Compare with Lemmon
Find recommendations
Writing
Write Thesis
Desimination Phase
Green Light Review
Defence